Observation of doubly excited resonances in the H^- ion

P. G. Harris,* H. C. Bryant, A. H. Mohagheghi, R. A. Reeder, and C. Y. Tang
University of New Mexico, Albuquerque, New Mexico 87131

J. B. Donahue and C. R. Quick
Los Alamos National Laboratory, Los Alamos, New Mexico 87545

(Received 26 March 1990)

SSCL-SR-1175A
SSC-EOI0017A

Laser photodetachment on a relativistic H^- beam has revealed several series of resonances in which both electrons are excited. These "bound states in the continuum" appear as dips in the partial production cross sections of various excited states of neutral hydrogen. We present here a detailed account of the experimental observation of the resonances and the results of fits of the measured yields to sets of Fano profiles. A simple analytic formula for the energy-level spacing in this quantum-mechanical three-body system is verified.

In this paper we report the observation of several series of high-lying ^1P resonances in the photodetachment cross section of H^-. The energy levels of these doubly excited states are shown to obey a simple and elegant analytic formula. We discuss here in greater depth the results presented earlier.[1]

We begin in Sec. I with a short discussion of the physical nature of the resonances, before describing our experimental technique in Sec. II. Section III presents the results of the data analysis. Details of the experimental apparatus and of the data reduction are presented in the two appendixes.

I. THEORY

A. Autodetaching resonances

One can think of the resonances in H^-, such as the ^1P Feshbach and shape resonances associated with $H^0(n=2)$, as having a core consisting of an excited hydrogen atom which is polarized by a second, outer, electron. This polarization results in a potential which supports one or more bound states. Upon the return of the core hydrogen atom to its ground state, the outer electron is ejected—hence the name "autodetaching." This basic system of a polarized excited core binding an outer electron is sometimes known as a "planetary" resonance. It should be noted that this simple picture, with an "inner" and an "outer" electron, is not always appropriate to describe doubly excited states; this is the case for some of the states under study in this paper.

B. Hyperspherical coordinates and ridge states

The nonrelativistic Hamiltonian for the two-electron system with fixed nucleus is (in atomic units)

$$H=-\tfrac{1}{2}\nabla_1^2-\tfrac{1}{2}\nabla_2^2-\frac{Z}{r_1}-\frac{Z}{r_2}+\frac{1}{r_{12}}\ , \tag{1}$$

where the nuclear charge $Z=1$ for H^-, r_1, and r_2 are the distances of the two electrons from the nucleus, and r_{12} is the separation between the two electrons.

We adopt the hyperspherical coordinates, defined as

$$\mathcal{R}=(r_1^2+r_2^2)^{1/2}\ , \tag{2}$$

$$\tan\alpha=r_1/r_2\ , \tag{3}$$

and

$$\theta_{12}=\cos^{-1}(\hat{\mathbf{r}}_1\cdot\hat{\mathbf{r}}_2)\ , \tag{4}$$

where $\mathbf{r}_1,\mathbf{r}_2$ are the radius vectors of the electrons, and $\hat{\mathbf{r}}$ represents a unit vector.

In these coordinates, the Schrödinger equation for the two electrons (with the nucleus fixed) is[2]

$$\left[\frac{d^2}{d\mathcal{R}^2}+\frac{5}{\mathcal{R}}\frac{d}{d\mathcal{R}}-\frac{\Lambda^2}{\mathcal{R}^2}-\frac{2C}{\mathcal{R}}+2E\right]\bar{\psi}=0\ , \tag{5}$$

where Λ^2 is Casimir's operator

$$\Lambda^2=-\frac{1}{\sin^2\alpha\cos^2\alpha}\frac{d}{d\alpha}\sin^2\alpha\cos^2\alpha\frac{d}{d\alpha}+\frac{L_1^2}{\cos^2\alpha}+\frac{L_2^2}{\sin^2\alpha} \tag{6}$$

with eigenvalues $\lambda(\lambda+4)$, where λ is an integer. The potential energy of the system is $V=C/\mathcal{R}$, where

$$C=-\mathcal{R}\left[\frac{1}{r_1}+\frac{1}{r_2}-\frac{1}{r_{12}}\right]$$
$$=-\frac{1}{\cos\alpha}-\frac{1}{\sin\alpha}+\frac{1}{(1-\sin 2\alpha\cos\theta_{12})^{1/2}}\ . \tag{7}$$

This definition of C agrees with that of Lin,[3] but differs by a factor of -2 from that of Macek[2] and of an earlier work by Lin.[4]

Since the hyperspherical radius $\mathcal{R}$ is simply a scale factor, the potential energy can be represented by C (sometimes known as the "effective charge"), which is a function purely of the hyperspherical angles θ_{12} and α. It may therefore be plotted as a surface, as shown in Fig. 1. The energy has minima at $\alpha=0$ and $\pi/2$; these give rise

 ©1990 The American Physical Society

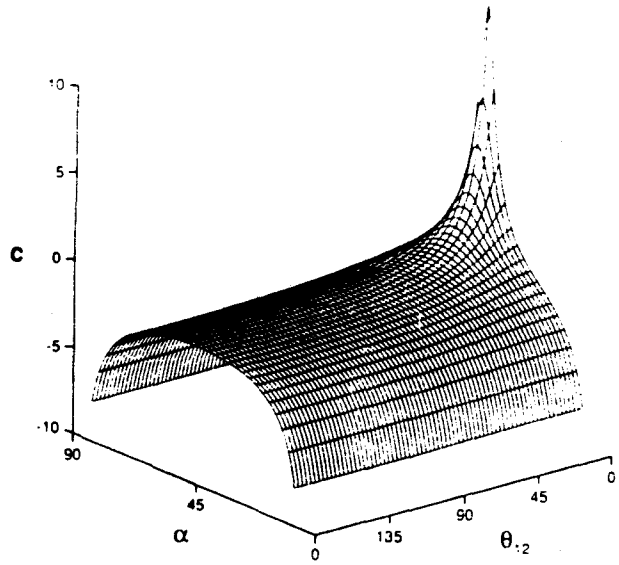

FIG. 1. Potential surface in hyperspherical coordinates at $\mathcal{R}=1$ bohr. [Courtesy of J. Knudson; based on a similar figure by Lin (Ref. 4).]

to the "valley states," for which one electron is close to the nucleus and the other is far away; this is a limiting case of the planetary resonances spoken of earlier. Singly excited states, in a system (such as helium) that supports them, would be valley states.

There is a singularity when the electrons are coincident, at $\alpha=\pi/4$, $\theta_{12}=0$. In addition, there is a saddle point at $\alpha=\pi/4$, $\theta_{12}=\pi$, which lies at the back of a broad, flat ridge; some states have a high probability density in this region of hyperspherical space—hence the nomenclature of the "ridge states" (see, e.g., Rau[5] or Lin[4]). At this saddle point, the electrons are equidistant from the nucleus and diametrically opposite one another, and their motion is strongly correlated; they therefore may lose their association with the parent hydrogen atom and become associated instead with the "grandparent" nucleus.

A whole series of these "ridge" states exists; in the lower limit, they are just the so-called intrashell resonances (both electrons occupying the same shell), characterized as $2s2p$, $3s3p$, $4s4p$, . . . (see Sec. I C); in the upper limit, they result in the double-detachment process. The ridge resonance energies obey a Rydberg-type formula which will be discussed in Sec. I E and again in Sec. III.

The Schrödinger equation (5) is not completely separable in hyperspherical coordinates. However, substitution of

$$\bar{\psi}=\mathcal{R}^{-5/2}\psi \tag{8}$$

reduces it to

$$\left[-\frac{d^2}{d\mathcal{R}^2}+\frac{\Lambda^2+\frac{15}{4}}{\mathcal{R}^2}+\frac{2C}{\mathcal{R}}-2E\right]\psi=0\ . \tag{9}$$

The wave function ψ can then be expanded[3,4] as

$$\psi=\sum_{\mu}\phi_{\mu}(\mathcal{R},\Omega)F_{\mu}(\mathcal{R})/(\mathcal{R}^{5/2}\sin\alpha\cos\alpha)\ . \tag{10}$$

The so-called *channel function* $\phi_{\mu}(\mathcal{R},\Omega)$ satisfies the differential equation

$$\frac{1}{\mathcal{R}^2}\left[-\frac{d^2}{d\alpha^2}+\frac{L_1^2}{\cos^2\alpha}+\frac{L_2^2}{\sin^2\alpha}+2\mathcal{R}C\right]\phi_{\mu}(\mathcal{R},\Omega)=U_{\mu}(\mathcal{R})\phi_{\mu}(\mathcal{R},\Omega)\ , \tag{11}$$

and the hyperradial function $F_{\mu}(\mathcal{R})$ satisfies the coupled equations

$$\left[\frac{d^2}{d\mathcal{R}^2}-U_{\mu}(\mathcal{R})+\frac{1}{4\mathcal{R}^2}+W_{\mu\mu}(\mathcal{R})+2E\right]F_{\mu}+\sum_{\nu}W_{\mu\nu}(\mathcal{R})F_{\nu}=0\ , \tag{12}$$

where the coupling terms W are defined as

$$W_{\mu\nu}=2\left\langle\phi_{\mu}\left|\frac{d}{d\mathcal{R}}\right|\phi_{\nu}\right\rangle\frac{d}{d\mathcal{R}}+\left\langle\phi_{\mu}\left|\frac{d^2}{d\mathcal{R}^2}\right|\phi_{\nu}\right\rangle\ . \tag{13}$$

At this stage, all of the nondiagonal coupling terms $W_{\mu\nu}$ are usually neglected; the resulting equation,

$$\left[\frac{d^2}{d\mathcal{R}^2}-U_{\mu}(\mathcal{R})+\frac{1}{4\mathcal{R}^2}+W_{\mu\mu}(\mathcal{R})+2E\right]F_{\mu}=0\ , \tag{14}$$

is known as the "adiabatic approximation." The second-order diagonal term $W_{\mu\mu}(\mathcal{R})$ is included in this approximation, although it is usually dropped in the Born-Oppenheimer expansion for diatomic molecules.

Each resonance series and its adjoining continuum are jointly called a "channel," each channel (designated by a set of parameters μ) being characterized by the eigenvalue $U_{\mu}(\mathcal{R})$ and its eigenfunction $\phi_{\mu}(\mathcal{R},\Omega)$.

C. Classification of doubly excited states

Having seen the origin of the potentials $U_{\mu}(\mathcal{R})$, we shall next consider the designations of the different channels μ. We begin in Secs. I C 1 and I C 2 with the simple $+$-$-$-0 designation (which primarily describes radial correlations), before looking at the more complete K-T-A classification in Sec. I C 3.

1. +-−-0 classification

Following the discovery of autoionizing resonances in helium,[6] Cooper, Fano, and Prats[7] developed a notation to describe doubly excited states. If the electrons were independent, with, say, one of the pair being in a $2s$ or $2p$ state, a series of excited states would arise from the other being in any of the higher states, n. As the electron correlations are very strong, however, linear combinations of these states are appropriate as a first approximation. So, for example, the wave functions ψ for the $^1P(S=0, L=1)$ resonances at the $H^0(n=2)$ threshold in H^- may be approximated in terms of the single-particle wave functions $u(n,l)$, by

$$\frac{1}{\sqrt{2}}[u(2s)u(np)\pm u(2p)u(ns)]\ , \tag{15}$$

represented more simply as

$$2snp \pm 2pns \quad . \tag{16}$$

In this case, the only + state supported is the so-called "shape" resonance [named for the curious shape, with three classical turning points, of the potential curve $U_\mu(\mathcal{R})$ that binds it], represented by $2s2p$. On the other hand, an entire series of − resonances is believed to be supported. The only one of these to have been observed so far[8] is the first in the series, the Feshbach resonance represented by $2s3p-2p3s$. Its first recursion should occur approximately 1 meV below the $n=2$ threshold.

In addition to the + and − channels, ^1P $n=2$ states may be formed from linear combinations of np and nd wave functions, but in this case the potential of the resulting "pd" or "0" channel is entirely repulsive, so no bound states are supported.

As we move to higher excited states, more such linear combinations become available to form ^1P states. The potentials $U_\mu(\mathcal{R})$ for $n=2-11$ are shown by Sadeghpour and Greene,[9] who also isolate the lowest + potentials and show the levels of the first resonance in each of these channels. These lowest + channels are also emphasized in Fig. 2, which shows potential curves[10] for $n=4-9$. Two-electron excitations into the + channels are expected to occur more strongly than into the channels by one to two orders of magnitude,[11] since the potential curves $U_+(\mathcal{R})$ are more attractive at small $\mathcal{R}$ and allow both electrons to overlap with the ground state far better than do the $U_-(\mathcal{R})$ curves.

In addition to emphasizing the lowest + potential curve in each channel, Fig. 2 also highlights a potential curve—the fourth 7+ curve—that may support a shape resonance just above the $n=7$ threshold. At the time of writing, it is not yet certain whether such a resonance is in fact bound here, but if it is it would be very broad, and probably rather weak, as it is associated with the fourth + series. It may mix with the lowest 8+ Feshbach resonance, which also lies right at the $n=7$ threshold.

Classifying the wave functions with + or − quantum numbers, which emphasizes whether the two electrons approaching the nucleus are in phase or out of phase[12]—and thus whether the wave function vanishes (for −) or not (for +) at $r_1=r_2$—is of course still an approximation. In fact, Eq. (15) should be a sum over all angular-momentum components l_1,l_2 that can add to a total $L=1$.[13] The hyperspherical calculations, however, treat the different channels (+, −, and pd) independently, by omitting the coupling terms $W_{\mu\nu}$ [Eq. (13)], and this seems to work well. The potential curves shown in Fig. 2 do not in fact cross one another. When they get very close, the coupling strength between them shows a sharp spike, and they repel one another. The region where this occurs is known as an "avoided crossing." From the coupling strength, one can tell if the two curves are decoupled enough to simply assume that they cross. In fact, the reason that the 2+ potential is repulsive at large $\mathcal{R}$ is that the + and − channels interact strongly enough to repel one another, so the + channel is pushed up (and supports the shape resonance) and the − channel is pushed down. As n increases, the avoided crossings become sharper and sharper, and the approximate + and − quantum numbers become more and more exact.

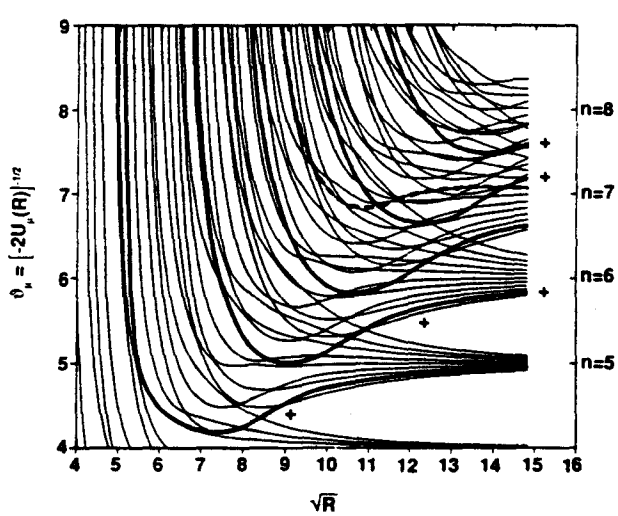

FIG. 2. Potential curves converging on the $n=4$ to 9 thresholds of H^0. (Courtesy of H. Sadeghpour.)

2. Mechanical analog

It is helpful to consider a simple classical model to explain the difference between the radial correlations of the electron pair for the + and the − types of resonance. Developing a model suggested by Cooper, Fano, and Prats,[7] Bryant proposed a mechanical analog based upon the "Newton's cradle"—the popular set of steel balls suspended, just touching, in a row, often used to demonstrate resonant behavior in classical mechanics. This model consists of just three such balls, the central one being extremely massive (to represent the proton) relative to the outer pair (the electrons), as illustrated in Fig. 3. There are two resonant modes of oscillation; the outer pair of balls may move either in the same direction (correlated motion), which results in a very long-lived resonance, or their motion may be "anticorrelated," which produces a short-lived resonance that begins to decay immediately, as the balls do not hit the central sphere simultaneously. These represent, then, the Feshbach (−) and shape (+) resonances, respectively. This analogy may be carried a stage further, as, in an external field, the outer electron in a −-type resonance would see a shielded nuclear potential, and so would be more susceptible to detachment, whereas for the +-type resonance both electrons would see the full nuclear charge when distant from the nucleus. Thus, the shape resonance, normally short-lived (and therefore broad), remains unaffected until relatively high fields are imposed, and in contrast the long-lived Feshbach resonance is quenched in modest fields.[14]

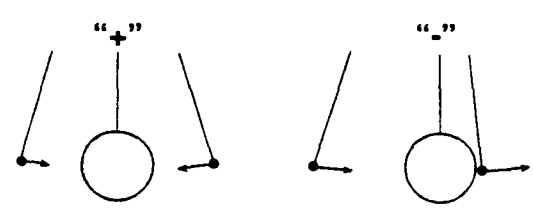

FIG. 3. "Newton's cradle" model of two-electron resonances.

3. K-T-A classification

An independent-particle model would represent the two-electron wave function as $|n_1 l_1, n_2 l_2, L, S, \pi\rangle$, where L and S are the total angular momentum and spin, respectively, and π is the parity. Herrick and Sinanoglu[15] introduced mixings of l_1 and l_2 within a given n_1, n_2 and replaced l_1 and l_2 with two new quantum numbers K and T. Each doubly excited state is then represented by quantum numbers $|n, m, K, T, L, S, \pi\rangle$, where m and n are the principal quantum numbers of the outer and inner electrons, respectively. n is therefore the hydrogenic threshold below which the resonance lies. The intrashell resonances, the lowest of any given series, have the two electrons occupying the same shell, so $m = n$.

The numbers K and T arise from group theoretical calculations. K is related to $\langle -\cos\theta_{12}\rangle$, where θ_{12} represents the angle between the radius vectors of the electrons; the larger the positive K, the closer is $\langle -\cos\theta_{12}\rangle$ to unity. K may be considered as a (bending) vibrational quantum number. T, on the other hand, measures the projection of the total angular momentum L onto the interelectron axis, and as such describes the orientations between the orbitals of the two electrons; thus, $T=0$ implies that the orbitals lie in the same plane. T may be considered to be a rotational quantum number. K and T, therefore, describe the angular correlations of the system.[16] According to Herrick and Sinanoglu, $T = 0, 1, \ldots, \min(L, n-1)$ (although $T=0$ is forbidden for states where the parity $\pi = (-1)^{L+1}$), and $K = n-T-1, n-T-3, \ldots, -(n-1-T)$.

The lowest $^1P^\circ$ + channels have the maximum possible K within a given n manifold, namely $n-2$, and also have $T=1$. In addition, Lin[12] introduces a quantum number A to describe radial correlations. A is allowed the values $+1$, -1, and 0. A state with $A=+1$ would have an antinode for the hyperspherical angle α [of Eq. (3)] at about $\alpha = \pi/4$; a state with $A=-1$ would have a node there. This designation coincides with the + or − classification of Cooper, Fano, and Prats. States that have neither node nor antinode are assigned $A=0$, and their characters are similar to singly excited states. A may also be expressed in terms of the other quantum numbers.[3] If $K > L-n$, then $A = \pi(-1)^{S+T}$; otherwise, $A=0$. In addition, states with $L > 2(n-1)$ must have $A=0$.

D. Recursion formula

Having established the nature of the potentials $U_\mu(\mathcal{R})$, let us now consider the energies of the bound states that they support.

Gailitis and Damburg[17] have shown that, as the hyperspherical radius $\mathcal{R} \to \infty$, the potential $U_\mu(\mathcal{R})$—which is just the interaction energy of an electron in the field of an excited hydrogen atom—takes the form (in eV)

$$U_\mu(\mathcal{R}) \to -R\left[\frac{1}{n^2} + \frac{a_n}{\mathcal{R}^2}\right], \tag{17}$$

where R is the (reduced-mass) Rydberg energy, 13.5984 eV (not to be confused with the hyperspherical radius $\mathcal{R}$), and the hydrogen atom is in state n. This is the long-range dipole potential that binds series of the so-called Feshbach resonances (of both + and − character) below the hydrogenic threshold in question, as we have discussed in Sec. I C 1 for $n=2$. The positions E_k and widths Γ_k of successive resonances within such a series, converging on the threshold at energy $E_n = E_t - R/n^2$ (where E_t is the double-detachment threshold energy, 14.3526 eV) should then obey the simple recursion formula

$$\frac{E_n - E_k}{E_n - E_{k-1}} = e^{2\pi/\alpha_n} = \frac{\Gamma_k}{\Gamma_{k+1}}, \tag{18}$$

where $k = m - n + 1$ is the "number" of the resonance in the series, and

$$\alpha_n = (a_n - \tfrac{1}{4})^{1/2}. \tag{19}$$

We shall refer to a_n as the *dipole parameter* of the relevant photoionization channel. The values of a_n may be calculated very precisely, and are listed for + channels in Table I; they may also be calculated approximately from the formulas[9]

$$a_n^+ = 3n^2 - \frac{23n}{3} + \frac{2}{3n} + 1 \tag{20}$$

for the lowest + series, and

$$a_n^- = 3n^2 - \frac{23n}{6} + \frac{7}{6n} \tag{21}$$

for the lowest − series. These approximations differ from the exact values by less than 0.3%, as shown also in Table I. The series are expected to terminate only when the resonances are separated from the threshold by an energy equal to the relativistic splitting of the hydrogenic levels.

Calculations[10] have shown that a strong series of +-type resonances lies below each hydrogenic threshold from $n=3$ upwards. (The series of Feshbach resonances believed to lie below $n=2$ is a − series.) Sadeghpour and Greene have to date carried their hyperspherical calculations up to the $n=12$ hydrogenic level.[9]

TABLE I. Theoretical values of the dipole parameter a_n^+. The thresholds in each case are those to which the resonances converge—e.g., the resonances in the $n=4$ continuum are associated with the hydrogenic $n=5$ threshold.

Hydrogenic threshold n	a_n^+ (theory)	a_n^+ (formula 2.20)
3	5.22	5.22
4	18.46	18.50
5	37.70	37.80
6	62.95	63.11
7	94.20	94.43
8	131.45	131.75
9	174.70	175.70
10	223.96	224.40

E. Recursions of series: the "2e formula"

Since the resonances are associated with the neutral hydrogenic thresholds, which themselves have an (approximate) energy dependence

$$E_n = E_t - R/n^2 \tag{22}$$

(where E_t is again the double-detachment threshold energy), it is natural to wonder if the entire series of resonances themselves might obey such a recursion relation. The so-called "modified Rydberg" formula

$$E = E_t - 2R\frac{(Z-\sigma)^2}{(n-\mu)^2} \tag{23}$$

for the lowest resonance in each series has been discussed by various authors, for example Read,[18] Rau,[19] and Molina;[20] the form essentially arises from the assumptions (i) that each electron partially screens the other from the charge of the nucleus, reducing the Coulomb potential outside the core from Z/r to $(Z-\sigma)/r$, where σ is a screening parameter, and (ii) that the stronger non-Coulombic potential experienced by an electron that penetrates the core may be parametrized by a quantum defect μ.

The formula may be obtained by considering the energy spectrum produced by the hyperspherical potential [see Eq. (7)] expanded about the saddle point (recall from Sec. I B that the lowest resonances in each + series, the intrashell resonances, essentially reside at this point). The expansion gives, in atomic units,[21,18]

$$V = \frac{1}{\mathcal{R}}[-Z_0 - Z_\alpha(\pi/4-\alpha)^2 + Z_\theta(\pi-\theta_{12})^2] , \tag{24}$$

where

$$Z_0 = 2\sqrt{2}(Z-\tfrac{1}{4}) ,$$

$$Z_\alpha = 3\sqrt{2}(Z-\tfrac{1}{12}) ,$$

and

$$Z_\theta = \sqrt{2}/16 ,$$

and of course $Z=1$ for H^-. A first approximation to the states localized around $\alpha=\pi/4$, $\theta_{12}=\pi$ is to retain only the "hyperspherically symmetric" part in Z_0. However, because the saddle is so flat, even a small energy-level spacing implies a significant extension in α and θ_{12} away from the saddle point; in other words, the wave function does not lie entirely on the ridge, but resides partially in the valleys. The quantum defect compensates in some ways for this "core" effect. It is introduced, together with the screening parameter, by inclusion of the Z_α and Z_θ terms in the expansion.

Sadeghpour and Greene[9,10] have fit the screening parameter σ and the quantum defect μ to their own calculations of the energies of the lowest + ^1P resonances in the $n=3$, 4, and 5 series. By combining the results with the dipole recursion formula and the Rydberg formula, they have produced an analytic expression for the energies of all of the +-type ^1P resonances in H^- associated with all of the hydrogenic thresholds,

$$E(n,m) = E_t - \frac{R}{n^2} + 2R\, e^{-2\pi(m-n)/\alpha_n}\left[\frac{1}{2n^2} - \frac{0.70784}{(n+0.377)^2}\right] , \tag{25}$$

where n is the principal quantum number of the hydrogenic threshold in question, $m=n,n+1,n+2,\ldots$, and α_n is the dipole parameter belonging to channel n. The first two terms are the usual Rydberg series for the hydrogenic thresholds (22). The term in large parentheses is the difference between these thresholds and the lowest resonance in each series as given by the modified Rydberg formula (23). This difference is multiplied by the factor $e^{-2\pi(m-n)/\alpha_n}$ to satisfy the dipole scaling law (18). Notice that the quantum defect μ is unusual in that it is negative—this may suggest a different origin than the postulated "core effect." Sadeghpour and Greene refer to Eq. (25) as the "two-electron formula," or, more simply, the "2e formula."

For future convenience, let us now define

$$\eta = (Z-\sigma)^2 , \tag{26}$$

so that in this case $\eta = 0.707\,84$.

F. Cross-section structure in the resonance region

So far, we have discussed the nature of the doubly excited states, the different ways of classifying them, and the relationships between their energy levels. We conclude Sec. I by considering how the resonances might affect the continuum photodetachment cross section, and what kind of structure we might therefore expect to see as we "tune" a laser through the resonance energies.

If we represent the amplitude of a resonant state as

$$\psi_R(t) = Ae^{-i\omega_0 t}e^{-t/2\tau} , \tag{27}$$

a Fourier transform into the energy domain gives

$$\psi_R(E) = \frac{ia\Gamma/2}{E-E_0+i\Gamma/2} , \tag{28}$$

where $\Gamma\tau=\hbar$, $E=\hbar\omega$, and $a=2A\hbar/\Gamma$.

This in turn leads to the usual Breit-Wigner formula for the cross section of a resonance,

$$\sigma = \psi^*\psi = \frac{a^2\Gamma^2/4}{(E-E_0)^2+\Gamma^2/4} , \tag{29}$$

where a constant of proportionality is included in the normalization.

If, however, the resonance lies in a continuum, then the total amplitude ψ_t becomes instead[14]

$$\psi_t = b + \frac{ae^{i\phi}\Gamma/2}{E-E_0+i\Gamma/2} , \tag{30}$$

where b is the continuum amplitude and ϕ is the phase difference between the resonance and the continuum. This leads easily to

$$\sigma = b^2 + \frac{a^2+2ab(\varepsilon\cos\phi+\sin\phi)}{\varepsilon^2+1} , \tag{31}$$

where $\varepsilon = 2(E - E_0)/\Gamma$.

If the resonances overlap one another, it is necessary to add their amplitudes before calculating the intensity $\psi^*\psi$, and thus one obtains

$$\psi_i = b + \sum \frac{ae^{i\phi}\Gamma/2}{E - E_0 + i\Gamma/2} . \tag{32}$$

(A summation index j is here implied but suppressed on the amplitude a, width Γ, phase ϕ, and energy E_0 of the resonances). The continuum background, here represented as b, also may be a function of the photon energy. When fitting to this model, it was assumed that b had a linear dependence on energy.

Equation (31) shows that the shape of the resonance depends on the phase ϕ between the resonance and the continuum. The resonances in question here are interesting in that the phase difference with the continuum is close to 180°—they therefore appear as dips rather than peaks. The dips found below $n = 3$ by Hamm *et al.*[22] are in fact combinations of a dip and a peak, suggesting that the phase difference with the continuum is close to 90°; the $n = 2$ Feshbach resonance appears as a peak (although it is believed to have a dip associated with it), indicating that it is nearly in phase with the continuum in this model.

It is interesting to speculate that if we could somehow separate out the excited states before they were to decay, perhaps by laser excitation to a higher resonant state, the measured partial cross sections would then be from continuum production alone, and the dips should disappear. This is similar to determining which slit a photon went through in a double-slit experiment, which destroys the interference pattern.

With a surprising amount of algebra, (31) may be cast in the more common form[23]

$$\sigma = \sigma_b + \sigma_a \frac{(q+\varepsilon)^2}{1+\varepsilon^2} , \tag{33}$$

usually known as a Fano line shape. Note that $b^2 \neq \sigma_b$, since as $\varepsilon \to \infty$, $\sigma \to \sigma_a + \sigma_b$; this would seem to imply that the resonance contributes a term σ_a to the continuum background even infinitely far from the energy E_0 of the resonance. Let us therefore redefine σ_b,

$$\sigma_b \to \sigma_b - \sigma_a , \tag{34}$$

so that the continuum amplitude far from the resonance is just σ_b. The resonance is then "decoupled" from the continuum, and the Fano line shape becomes

$$\sigma = \sigma_b + \sigma_a \left[\frac{(q+\varepsilon)^2}{1+\varepsilon^2} - 1 \right] . \tag{35}$$

A series of such line shapes that do not overlap would then be represented by

$$\sigma = \sigma_b + \sum \sigma_a \left[\frac{(q+\varepsilon)^2}{1+\varepsilon^2} - 1 \right] , \tag{36}$$

where again it is worth emphasizing that the σ_b defined here is slightly different from that defined by Fano.

The shape of the resonance, determined by ϕ in (31), is correspondingly contained in the asymmetry parameter q (33). This is defined as

$$q = \frac{\langle \Phi | T | i \rangle}{(\pi\Gamma/2)^{1/2} \langle \Psi | T | i \rangle} , \tag{37}$$

where $\langle \Phi | T | i \rangle$ is the transition probability from the H^- ground state i to the resonance, and $\langle \Psi | T | i \rangle$ is the transition probability from the ground state to the continuum. Since the overlap of the resonance wave function with the ground state is expected to become very close to zero for high-lying resonances, $q \to 0$, and the resonances should appear more and more like pure dips.

Early evidence for both the dipole recursion formula and for the diplike structure of high-lying resonances came from the first double-detachment experiment,[24] when dips were found in the $n = 5$ continuum, as shown in Fig. 4.[25] The scan was at coarse resolution, and the third dip was only represented by a single data point.

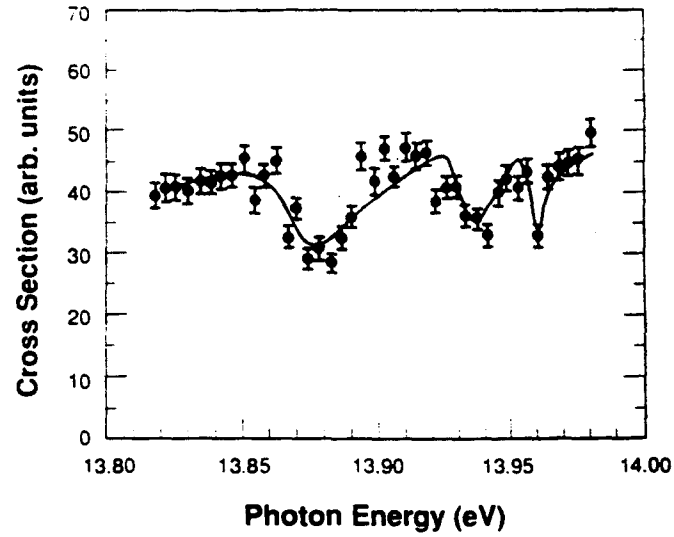

FIG. 4. Dips in the H^- continuum below $H^0(n=6)$. Threshold energies are 13.8084 eV for $n = 5$ and 13.9746 eV for $n = 6$.

II. EXPERIMENTAL TECHNIQUE

The experimental apparatus, of which there is a schematic diagram in Fig. 5, is described in Appendix A. Some familiarity with the material therein is assumed in this section, which aims to outline the principles underly-

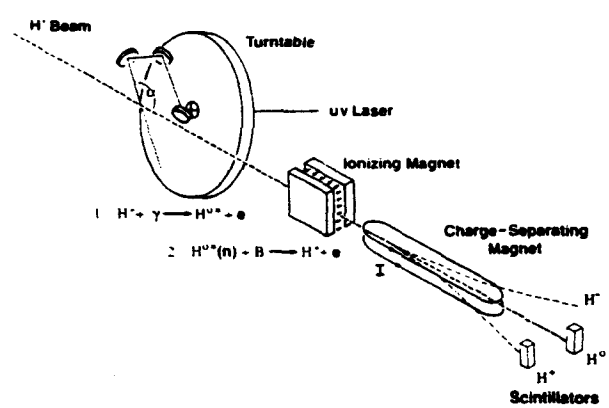

FIG. 5. Apparatus for high-lying resonances search.

ing the experiment and the procedures followed during the data taking. A detailed description of the apparatus and of the procedure followed in acquiring data is published elsewhere.[26]

A. Overview

The experiment described here is the latest in a series of studies of H^- that have been carried out at the Los Alamos Clinton P. Anderson Meson Physics Facility (LAMPF), a linear accelerator that provides a beam of H^- ions at energies up to 800 MeV ($\beta=0.842$). LAMPF is uniquely suited to such studies, since the relativistic nature of the beam provides two extremely powerful tools. First, and foremost, is the relativistic Doppler shift. As the H^- ions are moving at relativistic velocities, making them intercept a laser beam of laboratory photon energy E_0 at a varying angle α changes the barycentric photon energy E according to the formula

$$E=E_0\gamma(1+\beta\cos\alpha)\ , \tag{38}$$

where $\beta=v/c$ and $\gamma=(1-\beta^2)^{-1/2}$; $\alpha=0$ when the beams meet head on. The enormous range of tuning—over a decade for an 800-MeV beam—is otherwise totally out of the question for any lasers available either now or in the foreseeable future. Coupling this tuning ability with available lasers, from CO_2 through the various harmonics of a Nd:YAG (where YAG is yttrium aluminum garnet) to an excimer ArF, any photon energy from 0.03 eV up to 21 eV is attainable. This is a perfect match with the energy range of interest for H^-, from well below the single-electron photodetachment threshold, right through the resonance region and up beyond the double-detachment threshold.

The second important feature of the LAMPF beam is the relativistic transformation of electromagnetic fields. A modest transverse magnetic field $B_\perp$ in the laboratory becomes a substantial electric field, of strength

$$F_\perp=\gamma\beta cB_\perp \tag{39}$$

(SI units), in the rest frame of the ions. It is extremely difficult to apply such strong fields in a normal laboratory environment, especially to charged particles, as the several MV/cm that have been applied here. Thus, this technique allows the study, for example, of the quenching of resonances in extremely strong dc fields.

In order to study the high-lying resonances in H^-, which, as has been indicated earlier, lie at energies of 10–14 eV—in the far-uv region—the fourth harmonic of our Nd:YAG laser ($E_0=4.6595$ eV) is Doppler-tuned to excite the transition

$$H^-+\gamma\rightarrow H^{0*}(\le n)+e^-\ , \tag{40}$$

where the principal quantum number n of the hydrogen atom is typically between four and eight, and the $\le$ sign indicates that the atom may, instead, be excited to any state lower than n, with the electron carrying off the excess energy. The asterisk (*) indicates that the electron in the atom is excited.

As the angle α between laser and particle beams becomes smaller, and the photon energy correspondingly higher, successively higher n states are produced. If, however, the photon energy should match that of a resonance in the H^- continuum, then the process

$$H^-+\gamma\rightarrow H^{-**}\rightarrow H^{0*}(\le n)+e^- \tag{41}$$

may also take place. The amplitudes for excitation of the neutral hydrogen atom via production of the doubly excited resonant state H^{-**} [Eq. (41)] and that of direct excitation [Eq. (40)] will add coherently, resulting in structure on the continuum cross section as discussed in Sec. I F.

Let us consider a photon with a Doppler-tuned energy sufficient to detach the second electron from the H^- ion and to excite the remaining hydrogen atom into the state, say, $n=4$. There is a large probability that it will, instead, eject the outer electron and leave the neutral hydrogen in $n=1$, 2, or 3. If we wish to see structure in the H^0 ($n=4$) production continuum, it is essential that we discriminate against this background.

It is here that the transformation of (laboratory frame) magnetic fields into (barycentric frame) electric fields becomes important, for, by applying a field of ~4000 G, the corresponding field of 1.9 MV/cm in the ion's rest frame is sufficient to strip the electron from $H^{0*}(n=4)$, while leaving unaffected those atoms in $n\le 3$. The protons resulting from this so-called field ionization are magnetically separated from the remaining neutral and positively charged particles, giving a clear signal of the production of $H^{0*}(n=4)$.

We might expect, then, that as we increase the barycentric photon energy, starting from that needed to produce $H^{0*}(n\le 3)$, we should see a staircase-type structure, as shown in Fig. 6(a), with the onset first of $n=4$ production, then of $n=5$, 6, and so on. (This figure also includes a linear dependence with energy of the continuum cross section.) In addition, by reducing the magnetic field to the pont where it is no longer able to strip $H^{0*}(n=4)$, but is able to strip $H^{0*}(n\ge 5)$, we should again see a staircase structure, but this time beginning with the onset of $n=5$ production. Thus, we have the means to isolate and study a single channel at a time. This iterative process is repeated for successively higher n states until the signal becomes so small that it is impossible to discern the structure above the background noise.

The interference in the cross section, due to the coherent addition of amplitudes for the production of the H^{0*} continuum and the H^{-**} resonance (see Sec. I F), results in a series of "dips" in each $H^{0*}(n)$ channel, as shown schematically in Fig. 6(b), becoming progressively narrower and closer together as they converge on the $H^{0*}(n+1)$ threshold. The object of this experiment is to characterize these dips, measuring their positions and widths, and to compare them to the many predicted ^1P resonances in H^-.

B. Energy calibration

Transitions between excited states of neutral hydrogen are used to determine the energy scale. A neutralizing thin foil is used to produce excited H^0 atoms; scanning the magnetic field of an electron spectrometer shows us

the distribution of high-lying excited states. If a magnetic field of ≈ 130 G is then applied (*before* the laser interaction region), these high-lying states will be field ionized, and no longer detectable by the electron spectrometer. The laser-particle beam intersection angle may then be swept until the spectrometer, set at the appropriate field, once again detects high-lying states, this time promoted from lower excited states by the laser. For example, if the spectrometer is tuned to detect, say, the state $n=14$, and the magnet has stripped all of the foil-produced atoms in the state $n=14$, then the spectrometer will detect nothing until the laser angle is set to the transition from $n=1$ to $n=14$ (or $n=2$ to 14, etc.). The angular spacing between several such hydrogen lines tells us which lines we are looking at, and therefore where to expect other structure. The $n=2$ Feshbach resonance provides another important energy reference point. Instrumental resolution may be determined from the widths of the hydrogen lines and of the Feshbach resonance.[27]

The angular spacing between these hydrogen lines may appear to vary slightly from that expected for two reasons; firstly, if the laser is not properly aligned, it will "wander" as the intersection angle is varied; and secondly, runout in the bearings on the belt drive system will cause a sinusoidal variation from linearity in the encoder readout itself. As the structures under observation here all lie within a very small angular range, however, these variations are not generally a problem. A longer-term drift may be caused by a change in the frequency of the laser itself, by up to a wave number. This (systematic) shift in energy scaling is not apparent in any of the data.

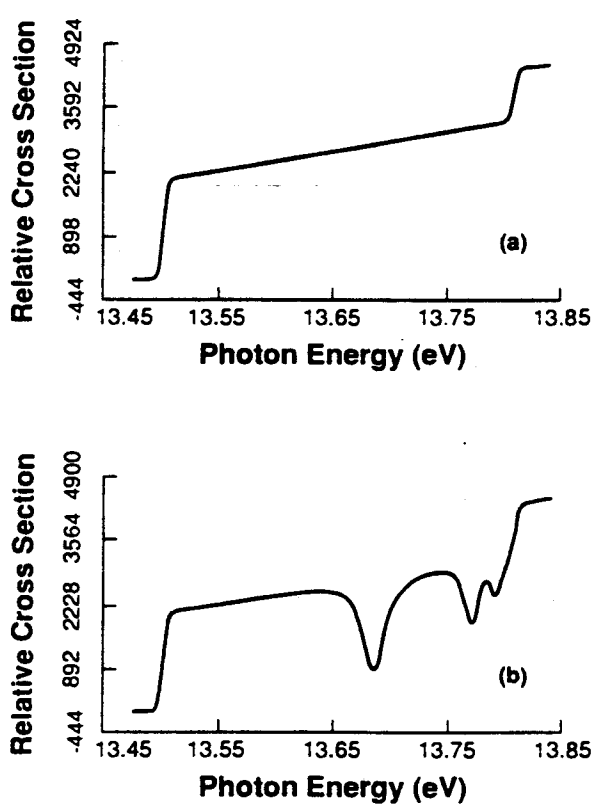

FIG. 6. Expected staircase structure of continuum, (a) without resonances, (b) showing dip resonances.

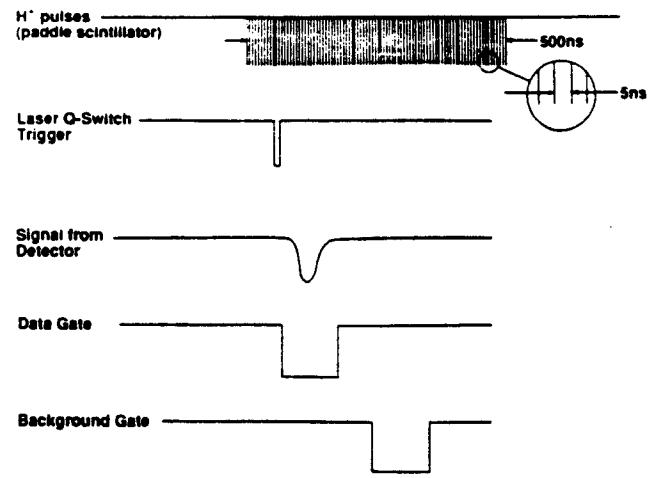

FIG. 7. Laser-particle beam timing overlap, with relative positions of data and background gates.

C. Taking data

During a run, the laser-particle beam interaction will take place at a number (usually 100) of different intersection angle settings. Signals are collected at each angle setting for a certain amount of time, determined by integrating the H^- current detected by a Faraday cup in the beam stop. At each laser shot, the integrated signals from the detectors are recorded on magnetic tape; at the end of each angle, the computer calculates the sum, the mean, and the standard deviation of the mean of these signals, writes the results to a data file, and records such information as the angle-encoder setting, magnetometer readings, and so on. It also generates histograms of signal versus angle number. Fast electronics, discussed in Ref. 26, are used to synchronize the laser pulse with the particle beam, and to digitize the signals from the detectors (see Fig. 7.)

III. RESULTS AND ANALYSIS

In this section we discuss the results of the data fitting under various constraints. Of these results, we shall place particular emphasis upon the fitted energies of the resonances, since several theoretical calculations of these energies are available. We shall find that we are unable to discriminate between the different theoretical approaches at this level of precision, but that the simple analytic "2*e* formula" [Eq. (25)], with the parameters η [Eq. (26)] and μ [from Eq. (23)] determined by a fit to the data, is able to predict the energies as well as any of the *ab initio* calculations.

A. Fitting the data

All of the data collected and analyzed are displayed elsewhere;[26] the procedure followed for data reduction is discussed in Appendix B. The data for each hydrogenic continuum channel studied ($n=4,5,6,7$) were combined to produce one set of data for each channel, displayed in Figs. 8(a)–8(d). Each contains at least three prominent resonances, which seem to converge on the next higher threshold ($n=5,6,7,8$, respectively). These resonances

appear primarily as dips, although there is still evidence of some asymmetry—the Fano q parameter [Eq. (37)] is in each case close to zero. Figures 8(a)–8(d) also show the results of the fits to sets of Fano profiles.

As explained in Appendix B, the data set for each channel was fit first to a set of independent resonances, in which the probability amplitudes ψ_i were added (in case of overlap) before calculating the cross section $\sigma = \psi^* \psi$ (see Sec. I F). The amplitude for the continuum background was allowed to be a linear function of energy. When the fitted widths indicated that there was in fact no significant overlap, sets of standard Fano profiles were used for the fitting. The sets of resonances were then fit to the dipole recursion formula (18), both with the dipole moment a_n as a free parameter and with it fixed at the value predicted by theory.

Theoretical considerations suggest that the asymmetry parameter q and the amplitude σ_a of the Fano profiles (35) should be constant (or nearly so) throughout the series of resonances.[28] Fits were also performed, therefore, with these constraints.

For each fit, a value is given for χ-squared per degree of freedom (χ^2/ν, or reduced χ^2). Confidence levels (CL; defined as the probability of χ^2 exceeding its calculated value) are also given where they exceed 0.01%; however, with ~100 data points, the confidence level drops off extremely rapidly for $\chi^2/\nu > 1$.

A Gaussian width corresponding to our resolution of 8.3 meV has been convolved into each fit. The energy scaling and resolution were determined from the positions and widths of the $n=2$ Feshbach resonance and of several hydrogen lines, as outlined in Sec. II C, and the absolute uncertainty in energy is less than 1 meV (with a relative uncertainty between points of less than 0.2 meV). This is sufficiently small that no energy uncertainty has been introduced into the fits. Of course, the energies in the unconstrained fits are free to "float," whereas those in the dipole-formula fits are tied to the threshold energies;

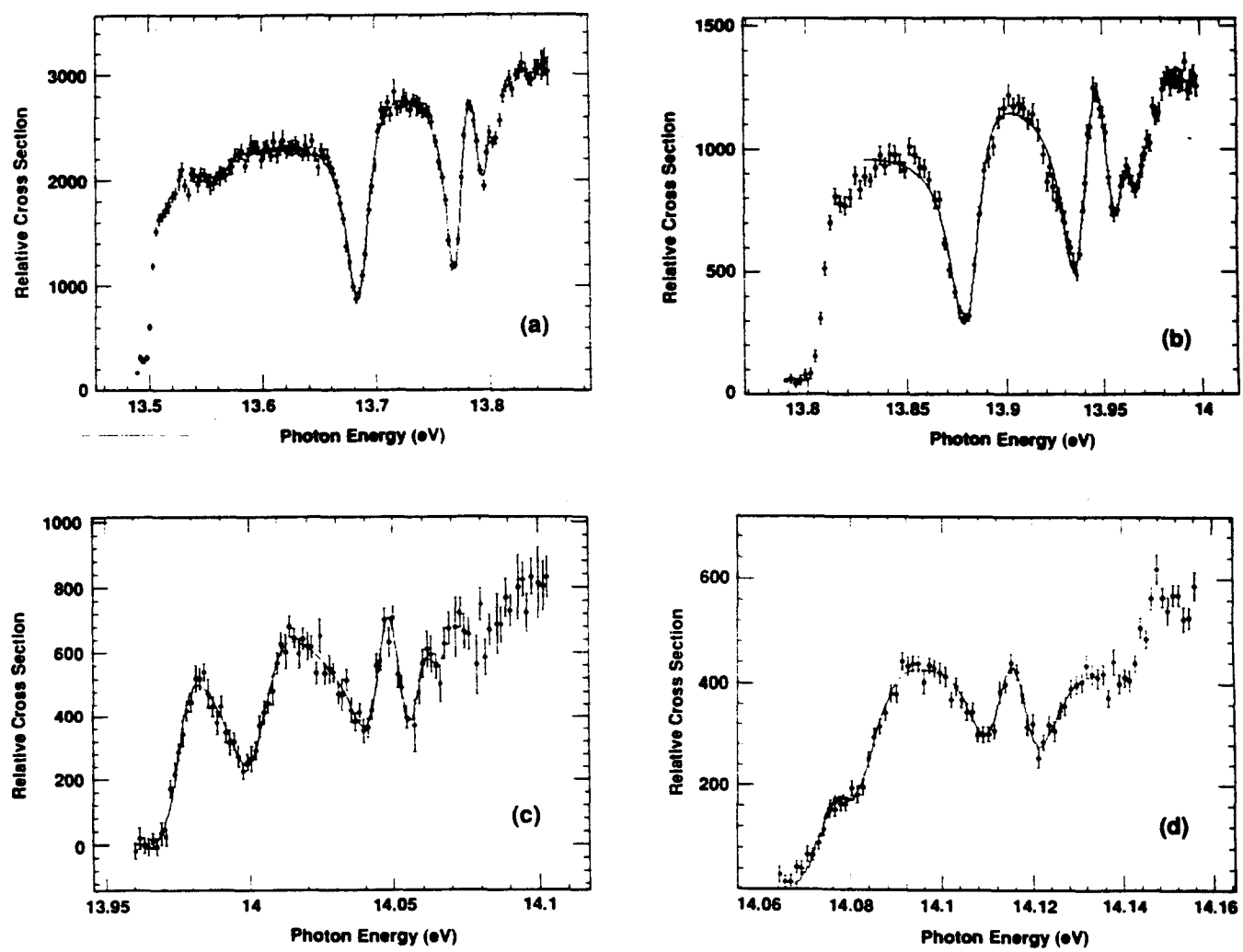

FIG. 8. Partial photodetachment cross sections of H^-, showing production of neutral hydrogen in (a) $n \geq 4$ ($\chi^2/\nu = 0.97$, CL is 55%); (b) $n \geq 5$ ($\chi^2/\nu = 1.85$, CL is 0.01%); (c) $n \geq 6$ ($\chi^2/\nu = 0.88$, CL is 73%); and (d) $n \geq 7$ ($\chi^2/\nu = 0.98$, CL is 50%). Instrumental resolution is 8.3 meV. Threshold energies as follows: $n=4$, 13.5054 eV; $n=5$, 13.8084 eV; $n=6$, 13.9746 eV; $n=7$, 14.0748 eV; $n=8$, 14.1398 eV. The solid lines are fits to sets of Fano profiles (see text).

but allowing an energy uncertainty in the dipole fits does not produce a consistent offset—either in magnitude or in sign—for the different channels, and does not bring about a large reduction in χ^2, and so the energy scale was fixed at its independently measured setting. The number of free parameters is in any case already prohibitive.

B. Positions and widths of the resonances

The fitted positions and widths of the resonances are given in Table II. Sets of Fano profiles were used throughout, the cross section of the continuum background σ_b being assumed to vary linearly with photon energy. The conditions under which the fits were performed are as follows.

(a) Positions of the minima, read from the data files.

(b) Unconstrained fits; parameters allowed to vary freely.

(c) Fits to dipole series [Eq. (18)]; dipole parameter a_n allowed to vary as a free parameter. Only the first resonance in each series is given, as the remainder are defined

TABLE II. Positions and widths of resonances.

(a) Positions of observed minima, by eye

Between thresholds	Position (eV)			
4 and 5	13.682	13.769	13.794	
5 and 6	13.879	13.936	13.955	13.966
6 and 7	13.997	14.039	14.057	
7 and 8	14.076	14.109	14.121	

(b) Unconstrained fits

Between thresholds	Position (eV)	Width (meV)	χ^2/ν (CL)
4 and 5	13.6858(3)	21.5(5)	0.97(55%)
	13.7708(3)	14.1(7)	
	13.7919(11)	14.3(7)	
5 and 6	13.8812(3)	11.6(8)	1.85(0.01%)
	13.9379(2)	8.2(5)	
	13.9557(1)	5.5(13)	
	13.9628(1)	1.0(4)	
6 and 7	14.0024(7)	12.4(13)	0.88(73%)
	14.0456(7)	4.9(9)	
	14.0558(2)	0.9(2)	
7 and 8	14.0802(10)	3.1(12)	0.98(50%)
	14.1132(2)	1.39(4)	
	14.1171(3)	1.13(6)	

(c) Dipole series fits; unconstrained a_n

Between thresholds	Position (eV)	Width (meV)	a_n	χ^2/ν (CL)
4 and 5	13.6864(1)	21.4(2)	31.3(2)	2.8
5 and 6	13.8817(1)	13.6(1)	47.5(3)	2.7
6 and 7	14.0016(3)	8.9(1)	73.7(13)	1.5(0.7%)
7 and 8	14.0800(9)	4.0(1)	110.1(46)	1.5(1.5%)

(d) Dipole series fits; a_n from theory (Table I)

Between thresholds	Position (eV)	Width (meV)	a_n	χ^2/ν (CL)
4 and 5	13.6879(1)	21.1(1)	37.70	4.9
5 and 6	13.8815(1)	14.0(1)	62.95	5.6
6 and 7	14.0020(4)	11.6(17)	94.20	1.7(0.06%)
7 and 8	14.0829(8)	4.0(3)	131.45	1.6(0.4%)

(e) Dipole series fits; a_n from theory; const q,σ_a

Between thresholds	Position (eV)	Width (meV)	χ^2/ν	q
4 and 5	13.6878(4)	19.8(7)	8.4	0.32(2)
5 and 6	13.8826(4)	11.6(6)	5.9	0.40(3)
6 and 7	13.9995(6)	14.0(14)	2.6	0.10(4)
7 and 8	14.0813(3)	4.0(2)	2.9	−0.09(4)

by the recursion formula.

(d) As for (c), but with the dipole parameter a_n fixed by theory (see Table I).

(e) As for (d), but with the values of the parameters q and σ_a assumed constant throughout the series of resonances.

Uncertainties in the fitted parameters are given in parentheses, and correspond to the change in the last significant digit required to increase the total χ^2 by one. This is a standard approach, although it clearly becomes invalid if χ^2/ν differs significantly from unity.

The position of the resonance at the $n=7$ threshold may be subject to additional uncertainty since it does not appear as a full dip; in other words, only half of the profile can be seen. There may also be a shape resonance at the $n=7$ threshold (see Sec. I C 1) interfering with it, although if it is there it should be weak.

C. Comparison of energies and widths with theory

We compare here the fitted energies and widths of the resonances with several theoretical predictions. We begin in Sec. III C 1 with the theoretical predictions for the energies of the lowest resonances in several different series, and we compare these numbers with the resonance energies found from the unconstrained fits, to see if we are observing resonances from more than one series in each continuum. Following this, we compare the fitted energies with the energies expected in a *single* series in each continuum, where we find that the match is considerably better. In this paper, "energy" refers to the photon energy (in eV) needed to reach the state in question from the ground state.

Section III C 2 discusses the fits to the dipole recursion formula. We then detour briefly in Sec. III C 3 to see how well the minima read from the data files, which we take as the locations of the resonances, match up with the dipole law.

Section III C 4 shows a plot indicating the linear dependence of the energy of the lowest resonance in each series (below the double-detachment threshold) on the hydrogenic principal quantum number n [see Eq. (23)]; values are found for the screening and quantum-defect parameters σ and μ. Section III C 5 uses these parameters in the $2e$ formula [Eq. (25)] to predict the positions of all (lowest series) + resonances from $n=3$ to 10.

Section III C 6 concludes the discussion of resonance energies with a brief summary.

Section III C 7 compares the fitted values of the widths, already touched upon briefly in Sec. III B, with some theoretical predictions.

1. *Theory versus unconstrained fits*

Some theoretical predictions for resonance energies are given in Table III. In each case, these are the energies of the first resonance in each series, the energies of the others following from the dipole recursion formula. The calculated values of Ho and Callaway,[16] Ho,[29] and of Koyama, Takafuji, and Matsuzawa,[30] were converted from the published energies in rydbergs (measured downwards from the double-detachment threshold, at 14.352 62 eV) by using the *infinite* Rydberg constant $R_\infty = 13.605\,698$ eV. This should be appropriate for +-type resonances, where the nucleus is "stationary" (see the classical analog of Sec. I C 2). The difference in photon energy in any case amounts to no more than 0.4 meV.

The fitted energies (from the unconstrained fits) are also included in the table. It appears that the first resonance in the lowest + series of each channel matches fairly well, but no others do, indicating that we are just seeing that lowest + series. The calculated widths of some of the other series of resonances are sufficiently large that we might expect to observe them; the fact that

TABLE III. Fitted photon energies of resonances (eV) vs calculated values for lowest resonances in each series of (1) Ho and Callaway (Ref. 16) and Ho (Ref. 29), (2) Koyama, Takafuji, and Matsuzawa (Ref. 30), and (3) Sadeghpour (Ref. 10). Again, uncertainties in fitted parameters corresponding to $\Delta\chi^2=1$ are in parentheses.

Between thresholds	Fitted	Calculated (1)	(2)	(3)
4 and 5	13.6858(3)	13.6846	13.6809	13.6857
	13.7708(3)	13.7574	13.7381	13.7369
	13.7919(11)		13.7675	13.7703
			13.7831	
5 and 6	13.8812(3)	13.8798	13.8794	13.876
	13.9379(2)	13.9202	13.9148	13.9196
	13.9557(1)	13.9710	13.9270	
	13.9628(1)		13.9432	
6 and 7	14.0024(7)	14.0008	13.9991	13.9996
	14.0456(7)	14.0254	14.0245	
	14.0558(2)	14.0544	14.0391	
7 and 8	14.0802(10)			14.0783
	14.1132(2)			
	14.1171(3)			

we do not implies that the resonances are weak, i.e., that σ_J is small.

Table IV lists the measured resonance energies—again from the unconstrained fits— and compares them with the calculated values of the lowest + resonance series in each channel. The calculations are from Sadeghpour,[10] and include both precise calculations using quantum-defect theory and estimates from the 2e formula [Eq. (25)], using his values of the parameters η [Eq. (26)] and μ as discussed in Sec. I E. The match in this case is obviously (qualitatively) extremely good throughout the entire range of energies studied, indicating that the structure that we see is due almost entirely to the lowest + series.[9]

2. Dipole recursion formula fits

The fits with energies and widths constrained to the dipole scaling law [Eq. (18); cases (c), (d), and (e) in Sec. III B] have a much higher χ^2, and therefore appear to be considerably poorer descriptors of the data than the unconstrained fits. However, the fitted energies of the resonances match the unconstrained fits very closely—within just a few meV in each case, as shown in Table IV. The widths do not match as well, as will be seen later.

According to a quantum-defect picture, the dipole scaling law holds exactly only if several short-range parameters are constant. One might infer from the fits, and particularly from the extremely large χ^2 values obtained when q and σ_a are held constant, that these parameters vary weakly with energy.

It appears, then, that the dipole scaling law is not quite exact. At this level of precision, however, it could be that the background continuum is not well represented by the linear energy dependence of this model, or else that other resonances are altering the cross section slightly. It is interesting to note that in each case, when the dipole parameter a_n is allowed to vary, the value obtained is significantly lower (by some 16–25 %; see Table II) than the theoretically calculated value.

3. Minima "by eye" versus recursion formula

Returning to the top of Table II, we have the positions of the minima of each resonance (as read from the data files) listed. If the parameter q were constant over the range of the series, the resonances would all have the same shape; if, then, the dipole recursion formula holds, we would expect that any set of equivalent points on the set of Fano profiles, and not just the centroids, should obey the same recursion formula. Testing this with the calculated values of a_n (Table I), we find a reasonably close agreement; the recursions of the first minima are in each case not more than a few MeV from the observed values. They are, however, outside the uncertainty limits, bearing in mind the 1 meV precision of the energy scale. This again suggests that either q is not quite constant, or that the dipole scaling does not quite work precisely, or both.

4. Lowest resonance in each series

According to the modified Rydberg formula (23), the energies of the lowest resonance in each series (as measured downwards from the double-detachment threshold) should be proportional to $1/(n-\mu)^2$. Thus, a plot of $(E_t-E)^{-1/2}$ versus n should—and indeed does—yield a straight line, as shown in Fig. 9. The energies used are those from the unconstrained fits [case (b) in Sec. III B]. Included in this plot is the first of the dips below $n=3$, at 12.650(4) eV.[22] The $n=2$ shape resonance is not included since its structure is different from the other lowest + resonances, which are all Feshbach-type resonances.

The fitted line is

$$(E_t-E)^{-1/2}=0.0765(22)+0.2299(5)n$$
$$=0.2299(5)[n+0.333(10)]\ , \qquad (42)$$

where as usual the uncertainties are given in parentheses. For this fit, the 1-meV absolute energy uncertainty was added to *each* of the fitted uncertainties listed in Table II; the reduced χ^2 was then 0.78, with a 50% confidence level.

TABLE IV. Fitted photon energies of resonances in eV; (1) unconstrained fits, (2) dipole formula fits vs calculated values (Ref. 9), using (1) quantum-defect theory, (2) the 2e formula [Eq. (25)].

Between thresholds	Fitted (1)	Fitted (2)	Calc. (1)	Calc. (2)
4 and 5	13.6858(3)	13.6879(1)	13.6857	13.6868
	13.7708(3)	13.7661	13.7730	13.7650
	13.7919(11)	13.7934	13.7963	13.7930
5 and 6	13.8812(3)	13.8815(1)	13.8760	13.8792
	13.9379(2)	13.9326	13.9347	13.9316
	13.9557(1)	13.9558	13.9575	13.9553
	13.9628(1)	13.9662	13.9671	13.9660
6 and 7	14.0024(7)	14.0020(4)	13.9996	13.9989
	14.0456(7)	14.0369	14.0382	14.0352
	14.0558(2)	14.0551	14.0566	14.0543
7 and 8	14.0802(10)	14.0829(8)	14.0783	14.0783
	14.1132(2)	14.1071	14.1064	14.1044
	14.1171(3)	14.1291	14.1217	14.1195

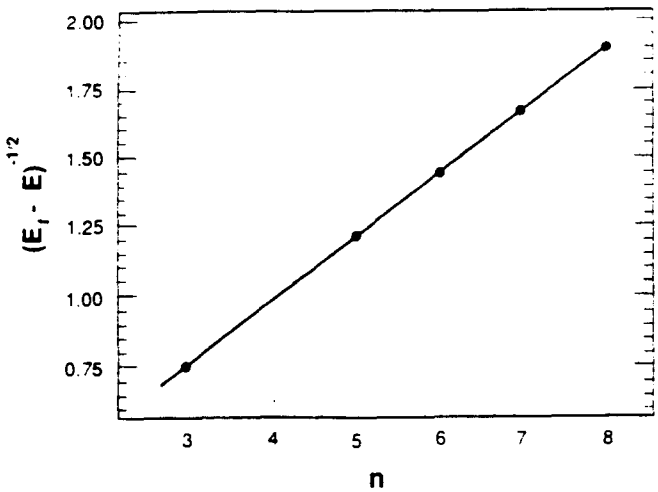

FIG. 9. A plot of the energy below the double-detachment threshold of the first resonance in each series, $(E_t - E)^{-1/2}$ vs the principal quantum number n. Error bars are too small to be visible on this scale.

5. *The 2e formula*

As discussed in Sec. I, the 2*e* formula [Eq. (25)]

$$E(n,m)=E_t-\frac{R}{n^2}+2R\,e^{-2\pi(m-n)/\alpha_n}\left[\frac{1}{2n^2}-\frac{\eta}{(n-\mu)^2}\right] \tag{43}$$

was fit to calculated energies of the lowest resonance in the hydrogenic $n=3$, 4, and 5 channels, giving values of 0.707 84 and -0.377 for the two parameters $\eta=(Z-\sigma)^2$ and μ, respectively. We can instead fit it to our measured resonance energies.

The 2*e* formula contains *two* assumptions—namely, the modified Rydberg formula for the lowest resonance in each series [Eq. (23)], and the dipole scaling law [Eq. (18)]. Fitting all of the resonances to the combined formula does not tell us *which* of the two formulas, if either, is at fault, and so has no value beyond the fits already performed on the formulas individually. We have already established that the dipole recursion formula is not exact (although it does seem to be a good qualitative predictor of the energies); building it into the fit, without allowing for the fact that it is an approximation (perhaps by increasing the error bars of all resonances beyond the first in each channel to a few meV) just weights the fit artificially in favor of the channels with more resonances (and therefore against the $n=3$ dips).

The most sound approach, then, is to fit just the *first* resonance in each channel—which of course we have already done in Sec. III C 4. The fitted line of Eq. (43) translates to values of η and μ of 0.6957(30) and $-0.333(10)$, respectively. Using these values, we may then predict (from the dipole recursion formula) the positions of the resonances, and since we have weighted the $n=3$ resonance appropriately, along with those of channels $n=5$ to 8, we may expect that the formula will hold over a wider energy range.

The predictions of the resonance energies are listed in Table V, beside the measured energies. Uncertainties in the calculated energies, which are listed for the first resonance in each series, are from the uncertainties in the fitted parameters η and μ, and so are *not* independent of the uncertainties listed for the measured energies.

A comparison of the measured energies with the 2*e*-formula predictions reveals that the energy of the second resonance in each series is consistently underestimated by 5–9 meV.

Figure 10 shows the 2*e*-formula predictions and the measured data for comparison. The data points are large enough to include the error bars. The ordinate is $(E_t-E)^{-1/2}$, following the format of Sadeghpour and Greene;[9] this effectively expands the energy scale—the few meV difference between the data and the curve for the second resonance in each series would be almost invisible on a normal scale covering the 1.5-eV range from the lowest $n=3$ to the highest $n=8$ resonance. The abscissa indicates the principal quantum number m of the

TABLE V. Fitted photon energies of resonances in eV (from unconstrained fits) vs calculated values from the 2*e* formula [Eq. (25)], using the best fit to the lowest resonance in each channel. The uncertainties in the calculated values arise from the uncertainties in the fitted parameters η and μ and are therefore *not* independent of the uncertainties in the measured energies. The thresholds n are those *to which the resonances converge.*

Threshold n	Fitted (eV)	Calc. (eV)
3	12.650(4)	12.6494(126)
	12.837(4)	12.8302
		12.8410
		12.8416
4		13.3448(64)
		13.4665
		13.4944
		13.5008
5	13.6858(3)	13.6874(38)
	13.7708(3)	13.7652
	13.7919(11)	13.7931
		13.8031
6	13.8812(3)	13.8809(25)
	13.9379(2)	13.9324
	13.9557(1)	13.9557
	13.9628(1)	13.9662
7	14.0024(7)	14.0008(18)
	14.0456(7)	14.0362
	14.0558(2)	14.0548
		14.0645
8	14.0802(10)	14.0801(13)
	14.1132(2)	14.1055
	14.1171(3)	14.1201
		14.1286
9		14.1354(10)
		14.1541
		14.1657
		14.1729
10		14.1754(8)
		14.1896
		14.1988
		14.2049

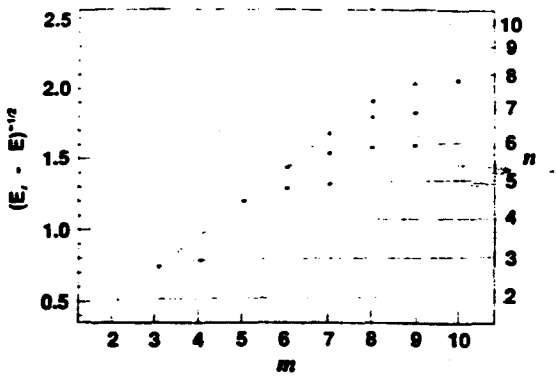

FIG. 10. The 2e-formula fit to the energies of the lowest resonance in each series (those lying on the dashed line).

outer electron; $m = n$ for the lowest resonance in each series (the intrashell resonances). Obviously, the curves have no physical meaning between integer values of m. The dashed line, on which the intrashell resonances lie, is exactly equivalent to the line of Fig. 9. Note that just *two* free parameters determine *all* of the curves shown.

6. *Summary of comparison of energies with theory*

The energies of the lowest resonances in each series seem to be well determined by a number of different theoretical calculations of varying complexity; disagreements between calculations typically amount to a few meV, and this is of the order of the differences between the calculated values and the experimentally measured values. The dipole recursion formula seems to hold approximately, as expected, within each series. The simple analytic 2e formula, based on this dipole scaling law and the modified Rydberg formula (23), predicts the positions of the resonances just as well as do any other calculations. Bearing in mind that each continuum partial cross section should contain many series of resonances, this remarkably good match seems to indicate that the lowest + series dominates every time, since otherwise the overlapping resonances would give a far more complicated spectrum.

7. *Comparison of measured widths with theory*

Table VI shows a comparison of the measured resonance widths versus theoretically calculated widths. The calculated widths are for the first resonance in each series, the remainder being given by the dipole recursion formula.

The width of the first resonance in each channel, from both the unconstrained fits and the dipole law fits, matches the calculated width (to within the error bars) *if* one assumes that the "uncertainty" in the calculated value is 1 in the last digit. Since the first resonance matches, subsequent resonances must match also for the dipole formula fits. Those of the unconstrained fits, on the other hand, seem to bear little relation to the widths expected from the dipole recursion formula, although there is a tendency for them to narrow as the next threshold is approached.

TABLE VI. Fitted widths of resonances in meV, (1) unconstrained fits, (2) fits to dipole series vs calculated values (Refs. 16 and 29). For the dipole-series fits and for the theoretical calculations, widths beyond the first are calculated from the dipole recursion formula. Widths considerably less than the 8-meV resolution may not be reliable.

Between thresholds	Resonance widths Fitted (1)	Fitted (2)	Calc.
4 and 5	21.5(5)	21.1(1)	20
	14.1(7)	7.56	7.2
	14.3(7)	2.7	2.6
5 and 6	13.0(3)	14.0(1)	13
	10.5(3)	6.3	5.9
	8.4(3)	2.9	2.7
	1.4(1)	1.3	1.2
6 and 7	12.4(14)	11.6(18)	11.1
	4.9(9)	6.1	5.8
	0.9(2)	3.2	3.0
7 and 8	3.1(1)	4.0(3)	
	1.39(4)	2.3	
	1.13(6)	1.3	

The third of the resonances converging to $n = 5$ seems to have a rather large width. This may be due to the existence of a fourth resonance in the series, the possibility of which will be discussed in Sec. III D 3 below.

With only four channels available for analysis, it is difficult to see any systematic trend of the widths. Those of the first resonances converging on the hydrogenic $n = 5$, 6, 7, and 8 thresholds are 22, 13, 12, and 3 meV, respectively (from the unconstrained fits), and no pattern is obvious from these four numbers. Since the dipole recursion formula appears to hold only approximately, precise calculations of widths of higher resonances in each series would be useful, but these do not seem to be available currently.

D. Other parameters

In this section we give the fitted values of the Fano asymmetry parameter q, the resonance amplitude σ_a, and the amplitudes and slopes of the continuum background.

1. *Asymmetry parameter q*

For cases (b) and (d) as outlined in Sec. III B, i.e., with the unconstrained fits and the fits to a series with the dipole moment fixed by theory, the value for the parameter q is given in Table VII. These should, however, be treated with some caution, because the apparent shapes of the resonances, which is really what q is measuring, are affected both by the shape of the underlying continuum (which has been assumed to have a linear dependence on energy) and by any other resonances that may be in the vicinity but which are not prominent enough to have been included in the fits. (It should be remembered that several series of resonances, of both + and − character, are expected in each channel, although the − resonances should not be significant.) Except for the first resonance

TABLE VII. Fitted values of the asymmetry parameter q for both unconstrained fits and for fits to dipole series of resonances.

Between thresholds	q_1	q_2	q_3	q_4
	Unconstrained fits [as in Table II(b)]			
4 and 5	0.187(14)	0.323(37)	−1.20(11)	
5 and 6	0.262(4)	0.406(3)	−0.064(13)	−0.957(54)
6 and 7	0.456(52)	1.23(21)	0.315(67)	
7 and 8	−0.09(15)	0.650(15)	−0.660(33)	
	Dipole series fits [as in Table II(d)]			
Between thresholds	q_1	q_2	q_3	q_4
4 and 5	0.292(6)	−0.081(4)	−0.193(21)	−0.863(16)
5 and 6	0.268(5)	−0.038(8)	−0.206(39)	−0.51(10)
6 and 7	0.360(32)	0.008(49)	−0.391(49)	−2.00(7)
7 and 8	0.28(12)	−0.18(7)	−0.317(47)	−2.0(3)

in the $n=5-6$ channel, agreement between the different estimates of q is poor.

The values of q for case (e) in Sec. III B, where q and σ_a are held constant, are given with the results in Table II; however, the extremely large values for the reduced χ^2 values show that the fits are extremely poor, and therefore that this model fails to represent the true structure. It will not be considered further.

2. *Resonance amplitudes σ_a*

Resonance amplitudes σ_a are given in Table VIII, as a fraction of the fitted continuum amplitude A (see Sec. III D 3), for the unconstrained fits and for the fits to the dipole recursion formula. There does not seem to be a consistent pattern to these amplitudes, except that they tend to be close to 1.0. Physically, they cannot be larger than 1.0 if $q=0$, since this would imply that the dip is *deeper* than the continuum background (neglecting the contribution to the continuum background of the *slope*, discussed in the Sec. III D 3). This constraint, however, is not build into the fits.

3. *Background amplitudes and slopes*

For each series of Fano profiles, the continuum background σ_b (36) was modeled by a linear function of energy,

$$\sigma_b = A + B(E - E_n)\ , \tag{44}$$

where E_n is the threshold energy (in eV) for the continuum channel in *which the resonances are embedded*—in other words, the $n=4$ threshold for the resonances converging on $n=5$, and so on.

As discussed in Appendix B, an attempt was made to approximate the cross-section units to μa_0^2 by using a $1/n^3$ scaling law, and so the quoted units of continuum amplitude are μa_0^2. Based on the scaling law and on the expected photodetachment cross section into $n=1$, the expected continuum amplitudes are ~2102, 1076, 623, and 392 μa_0^2 for the channels converging on $n=5$, 6, 7, and 8, respectively. It should be noted, however, that we are really only listing relative cross sections, and the quoted units of μa_0^2 should in no way be regarded as an absolute measurement.

Table IX lists the amplitudes A and slopes B of the continuum background. Although the slopes are relatively small, they appear to be essential to the fits, in that the reduced χ^2 values increase dramatically if the slopes are fixed at zero. The agreement between the unconstrained fits and the dipole scaling law fits is poor for both the background amplitudes and slopes (except for the background amplitude between the $n=5$ and $n=6$ thresholds).

E. Other possible resonance structures

We discuss here some structures that appear in the yield curves that may be due to resonances, but which are not as clearly defined as those discussed in the preceeding sections.

1. *The $n=9$ threshold + resonance candidate*

The fitted $2e$ formula predicts that the first + resonance associated with the $n=9$ threshold will occur at

TABLE VIII. Fitted values of the resonance amplitude σ_a as a fraction of the background amplitude for (1) unconstrained fits [as in Table II(b)], and (2) dipole recursion fits [as in Table II(d)].

Between thresholds	Resonance amplitudes σ_a (1)	(2)
4 and 5	0.948(14)	0.717(1)
	1.124(40)	1.036(10)
	0.845(45)	1.016(11)
5 and 6	0.951(12)	0.881(9)
	1.034(8)	1.117(24)
	1.424(6)	1.090(33)
	1.277(5)	0.95(13)
6 and 7	0.621(43)	0.72(6)
	0.517(57)	0.76(10)
	4.4(8)	0.92(21)
7 and 8	1.40(7)	1.02(7)
	2.88(11)	1.26(10)
	3.56(28)	2.20(30)

TABLE IX. Fitted values of the continuum amplitude (in units of approximately μa_0^2) and slope (in units of approximately μa_0^2/eV) for (1) unconstrained fits [as in Table II(b)], and (2) dipole recursion fits [as in Table II(d)]. See Sec. III D 3 for a discussion of the units.

Between thresholds	Continuum amplitudes (units of μa_0^2) (1)	(2)
4 and 5	2074(22)	2398(5)
5 and 6	1021(8)	1013(7)
6 and 7	712(25)	608(29)
7 and 8	473(28)	354(17)

Between thresholds	Continuum slopes (units of μa_0^2/eV) (1)	(2)
4 and 5	3975(65)	3579(17)
5 and 6	1858(39)	539(15)
6 and 7	−1665(53)	−1075(454)
7 and 8	−538(416)	1676(353)

14.1354 eV, just 4.4 meV below the $n=8$ threshold. As such, it should decay into the $n=7$ channel. The $n=7$ continuum fits discussed earlier were terminated at 14.136 eV, since at this energy (with 8.3 meV resolution) the $n=8$ production threshold should begin to influence the cross section.

Inspection of the entire energy range, however, shows a dip just before the $n=8$ onset. It is not a large dip, as the first resonances in each series have been in all other cases, but that may be expected of an $n=9$ threshold + resonance (9+) coupling to the $n=7$ continuum.

Figure 11 shows a fit of this entire range up to the $n=9$ threshold. The parameters representing the first three resonances were held constant at the values previously found in the unconstrained fits. The amplitude and slope of the $n=7$ continuum were allowed to vary, and the $1/n^3$ scaling law was assumed to hold between the $n=7$ and $n=8$ continua. The fitting routine was then asked to find a resonance corresponding to the dip between 14.13 and 14.15 eV. It produced the following parameters, with a reduced χ^2 value of 1.9:

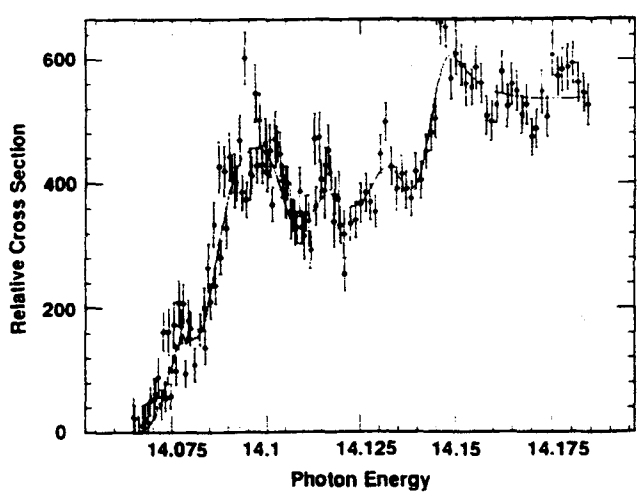

FIG. 11. $H^0(n=7,8)$ continuum production.

$$E_0 = 14.1429(1)\ \text{eV}\ ,$$

$$\Gamma = 0.9(2)\ \text{meV}\ ,$$

$$\sigma_a = 1.8(14)\ ,$$

$$q = 0.91(8)\ ,$$

$$A = 425(6)\mu a_0^2\ ,$$

$$B = 846(110)\ \mu a_0^2/\text{eV}\ .$$

Again, the amplitude σ_a of the resonance is given as a fraction of the continuum amplitude A. The fitted width may be unreliable as it is much less than the instrumental resolution. As before (Sec. III D 3), although units of μa_0^2 are quoted, A and B should not be regarded as absolute measurements.

The centroid of the dip is not quite in the expected place, although there is undoubtedly interference between the $n=8$ production threshold (which does appear to have a slightly delayed onset) and the resonance itself, in addition to any other resonances in the vicinity (from the 8+ series). It seems quite feasible that this shallow dip is in fact the first 9+ resonance. However, a fit to the 9+ series failed to find resonances in the right place for recursions of this first dip (the best fit had $\chi^2/\nu=3.6$). Further investigation of this structure is highly desirable. Note that the continuum amplitudes for $n=7$ and 8 seem, at least visually, to match the $1/n^3$ scaling law quite well.

2. $n=4$ threshold dip

There appears to be a shallow dip just above the $n=4$ production threshold, centered at about 13.55 eV [see Fig. 8(a)]. This dip is not very well defined, and its shape is not consistent from run to run; however, it does appear to be present in all of the runs that cover the appropriate energy range. Its nature is unknown; a shape resonance is possible above $n=4$, but if it exists it is expected to be extremely narrow. An alternative possibility is the "tail end" of a broad Feshbach resonance that is expected to lie *below* the $n=4$ threshold.[16] It was not included in this analysis because of its lack of consistency.

3. Fourth $n=5$ dip

Most of the zero-field runs that cover the range between the hydrogenic $n=4$ and $n=5$ thresholds show a small dip, or at least a plateau, just below the $n=$ threshold (at 13.8084 eV). It is generally within the noise and often represented by a single data point, but it does appear to repeat. It was not included in the fits because firstly, it is not well defined in any run; secondly, it is too close to the $n=5$ threshold (bearing in mind that our resolution is 8.3 meV); and thirdly, it is not clear that it is a resonance in its own right rather than just a return to the continuum level after a "dip-peak" asymmetric resonance preceeding it. Obviously there would be little meaning to a fit of such a structure to four free parameters.

TABLE X. Resonances in each series, numbered from the lowest (i.e., as $m-n+1$) that are quenched by a given electric field. Square brackets indicate that a given resonance is significantly suppressed (~50% reduction in depth of the dip) but not fully quenched.

Between thresholds	Electric field (kV/cm) 12	25	63	87
4 and 5	3		[2]	2
5 and 6		3	2	1
6 and 7	3[2]	2[1]		

F. Effects of electric fields

Electric fields were also applied to the interaction region, to study the quenching of the resonances. The polarization of the light was a mixture (approximately 50%–50%) of π and σ (parallel and perpendicular to the field). The fields, perpendicular to the plane of interaction of laser and particle beams, were produced by applying a potential difference between a pair of steel disks held 1 cm apart across the interaction region; the electric field F' in the barycentric frame is then γ times the field F in the laboratory frame. (A fairly weak magnetic field, of strength $B_\perp=\gamma\beta F_\perp/c$, is also produced by the relativistic transformation of the electric field; this amounts to no more than 250 G.)

The data from the electric-field runs are displayed elsewhere.[26] The effects of the fields are twofold; firstly, to quench the resonances; and secondly, to shift the thresholds downward in energy (and to change their shape).

Table X indicates the resonances that are quenched in given electric fields. Background levels caused problems, and the quality of much of the data is not optimum. Nonetheless, the quenching process is clearly demonstrated for all but the very strongest resonance (the first in the series below the hydrogenic $n=5$ threshold). There does not appear to be any appreciable change of shape (or shift in energy) of the resonances, as might have been expected from mixing, prior to the quenching.

The threshold shifts, probably due both to field-assisted tunneling from the ground state of H^- and to the changing of the threshold shapes by the linear Stark effect, are also visible in the data. Unfortunately the changing shapes of the thresholds, and the existence of structure below them, makes it difficult to pinpoint the onset of production. From a fairly clear step function at zero field, the threshold smears out into a slope as the linear Stark effect splits the degenerate levels into the different parabolic substates.

TABLE XI. Downward shifts in energy (meV) for the various production thresholds of neutral hydrogen.

Threshold \ Threshold shifts (meV) Electric field (kV/cm)	25	63	87
4	30(5)	45(10)	55(10)
5	35(10)	45(10)	60(20)
6	35(10)		

Table XI lists the approximate shifts in the threshold energy of $n=4$, 5, and 6 as the electric fields are applied. These are measured from the base of the (zero-field) step to the base of the (field-induced) slope.

IV. CONCLUSION

A century has passed between the first spectroscopic studies of atomic hydrogen and the current investigations of the negative hydrogen ion. Balmer discovered a simple recursion formula that predicted almost exactly the energies of the excited states of the hydrogen atom; now we are able to confirm a similar recursion formula for the energy levels of the doubly excited states in H^-:

$$E(N,n)=E_t-\frac{R}{n^2}+2R\,e^{-2\pi(m-n)/\alpha_n}\left[\frac{1}{2n^2}-\frac{0.696}{(n+0.333)^2}\right]. \tag{45}$$

This semiempirical formula is not a firm theoretical predictor, but it is an extremely good qualitative guide to the energies of the observed resonances.

The doubly excited states investigated in this study appear to be, in each case, series of Feshbach-type resonances associated with the hydrogenic thresholds below which they lie. They are due entirely to electron correlations. The good agreement with ongoing theoretical calculations of their energies seems to indicate that we are observing the lowest-lying resonances of + character, and their recursions. The lowest lying in each series, for which $m=n$, is a so-called *ridge resonance*, for which the two electrons are entirely equivalent; the recursions represent a series of states which become increasingly "planetary," as one electron with the nucleus forms a core about which the other orbits, until finally the limit of an excited hydrogen atom with the additional electron in the continuum is attained.

Calculations of the widths of the resonances are not so abundant, but those that are available also seem to be in good agreement with the data. Calculations of the cross sections, however, appear to be nonexistent. This makes fitting the data to theory more difficult, since not only the nature of the resonances but also the form of the underlying continuum in which they are embedded is unknown to us.

Fits of the resonances that are unconstrained yield energies that are very slightly different (a few meV) from those fit to the dipole recursion formula (which is built-in to the 2*e* formula above),

$$\frac{E_n-E_k}{E_n-E_{k+1}}=\varepsilon^{2\pi/\alpha}=\frac{\Gamma_k}{\Gamma_{k+1}}\ ; \tag{46}$$

the quality of the latter fits are, however, considerably worse than those of the former. It is conceivable that the dipole recursion formula is not working precisely, but it also seems quite possible that the shape of the underlying

continua are being distorted by the presence of weaker resonances.

The energy range included in this study was from the production threshold of $H^0(n=4)$ up to that of $H^0(n=8)$. (Some data were taken up to the $n=9$ threshold, but the signals were too small and noisy to observe structure.) The region between $n=7$ and $n=8$ is of particular interest; the first resonance associated with $n=8$ lies right at the $n=7$ production threshold, and so in channels higher than this the first resonance of each series should be "displaced" by a channel. Future explorations could also make the link with the previously studied resonances near the $n=2$ and 3 thresholds, by investigating the region between $n=3$ and 4.

ACKNOWLEDGMENTS

The authors would especially like to thank Hossein Sadeghpour and Chris Greene for considerable assistance in the interpretation of our data. We also acknowledge technical support, in particular from Lawrence Quintana and Afton Kirby and from Jim Hontas and Jesus Sanchez. We are grateful for the assistance of many others, including Dan Rislove, Jim Stewart, Hossein Tootoonchi, Hassan Sharifian, Win Smith, Stanley Cohen, Tom Altman, and Jim Knudson. This work was performed under the auspices of the U.S. Department of Energy, and was supported in part by the Division of Chemical Sciences, Office of Basic Energy Sciences, Office of Energy Research, U.S. Department of Energy. One of us (P.G.H.) would like to thank Los Alamos National Laboratory for financial support.

APPENDIX A: EXPERIMENTAL DETAILS

The beamline equipment, illustrated in Fig. 12, includes apparatus for all of our current experiments. An overview is given here of each component, beginning with the characteristics of the H^- beam itself.

1. The H^- beam and the high-resolution atomic beam facility

The LAMPF linac provides a H^- beam of 120 macropulses per second, each lasting for up to 700 μs, and each in its turn consisting of many micropulses spaced a minimum of 5 ns apart. The use of choppers allows considerable flexibility in the spacing (and therefore intensity) of the micropulses, depending upon the needs of the users.

The high-resolution atomic beam (HiRAB) experimental area at LAMPF is a dedicated atomic physics facility. Since the cross sections for atomic physics processes are extremely large in comparison with those of nuclear physics, very low beam currents are required. Because HiRAB was the primary user, the temporal structure of the beam was tailored to its needs, so the macropulses were compressed to just 500 ns instead of the normal 700 μs. The peak intensity of each micropulse was therefore higher, allowing the average current to be held correspondingly lower, typically in the range 1–50 pA. The kinetic energy of the beam was nominally 800 MeV, with our measurements[27] yielding an actual value of 797.3±0.3

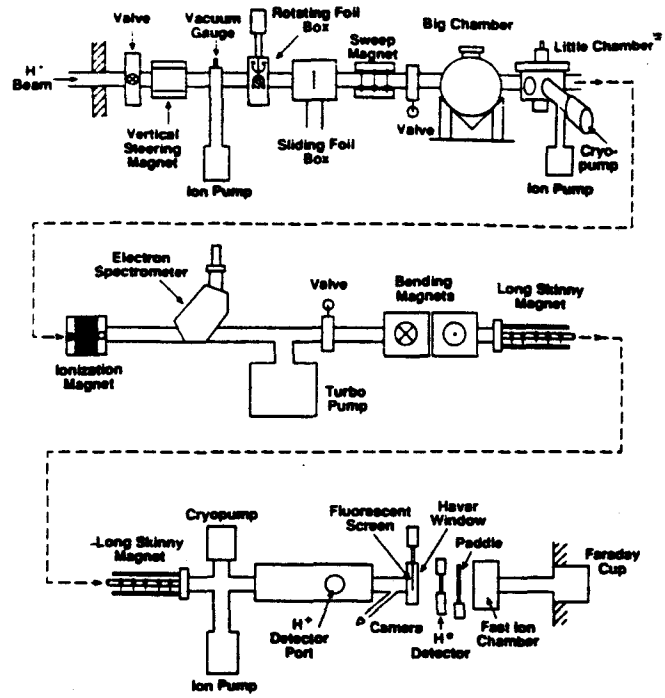

FIG. 12. Schematic diagram of beamline apparatus.

MeV mean kinetic energy, with a momentum spread $\delta p/p = 5\times10^{-4}$.

The divergence of the beam in the vertical direction may be limited, by dedicated strippers, to less than 10 μrad. The necessity for extensive steering prohibits achieving a similar level of collimation in the horizontal plane.

The HiRAB facility includes a large vibration-isolation slab, made of concrete on a bed of sand. Studies[31] have shown this to be effective in considerably reducing motion from heavy plant operations going on elsewhere, although the optical tables showed an unfortunate tendency to resonate at low frequencies.

2. Nd:YAG laser

The resonant structures in the H^- continuum lie at energies of 10.9–14 eV above the ground state. These high energies mean that, even with the Doppler-tuning facility, it is necessary to use ultraviolet photons. We used the fourth harmonic of a Q-switched Spectra Physics DCR-2A Nd:YAG laser, which has a wavelength of 266.1 nm.

The laser beam is 8 mm in diameter, with an estimated divergence of 0.5 mrad. The temporal structure of the laser pulse was monitored by a fast vacuum photodiode, the output of which was observed on a fast oscilloscope.

The harmonics were separated by a quartz Pellin-Broca prism on the optical table, the ultraviolet light then following the optical train via a succession of dielectric mirrors and into the larger of the two scattering chambers. Transmitting optics were all made of fused quartz.

The harmonic-generating crystals, in particular for the fourth harmonic, are sensitive to the angle of the incident

laser beam. The tuning of this angle was done by turning the ammonium dihydrogen phosphate harmonic-generation crystals remotely with a pair of stepper motors.

3. Foils

Two specially designed vacuum boxes (known as the *rotating-foil box* and the *sliding-foil box*, described in detail elsewhere[26]) held our neutralizing foils, the majority of which consisted of vacuum-deposited carbon of thicknesses 15–300 $\mu g/cm^2$. Steppermotor-driven actuators allowed the foils to be remotely inserted to and removed from the beamline. The foils were used to produce a H^0 beam for energy calibration.

4. Big Chamber

The Big Chamber is the first of the two laser–H^--beam interaction chambers. Inside it, a mirror system consisting of three (1-in. 45° angle-of-incidence) dielectric mirrors, is mounted on an optical bench; this in turn is attached to a turntable, allowing rotation in the vertical plane. The laser beam follows the axis of rotation—horizontal, and perpendicular to the H^- beam—into the chamber, where the first mirror deflects it to one side; the second mirror turns it to become parallel to the axis, and the third turns it in to the point where the axis of rotation intersects the H^- beam. Rotation of the turntable thus changes the angle of intersection of the laser and particle beams, providing Doppler tuning as illustrated schematically in Fig. 5.

The turntable is belt-driven. The 0.5-in.-wide steel belt, made from 0.005-in.-annealed 304 stainless-steel shim stock cut to length and laser welded, passes around a 1.000-in. drive shaft, giving the turntable a 10-to-1 step-down gear ratio. The shaft, coupled to a vacuum feedthrough, is driven by a stepping motor (200 steps per revolution) via a 100:1 gearbox. The motor takes a total of 2×10^5 steps per revolution of the turntable, which is equivalent to a step size of 31 μrad.

A 14-bit encoder (BEI model 5V 242 BX), also coupled to the turntable by a steel belt, measures the angle with a nominal precision equal to the 31-μrad step size. In 1988, the number of encoder steps for a complete revolution was measured, and found to be 198 777.7, by aligning a mark on the turntable with the crosshair in a telescopic sight and turning the turntable until the mark lined up again. This figure implies an average of 552.16 steps/deg, but over any given region there will be some variation from this figure from bearing runout. Because the encoder makes 12.2 revolutions as the turntable turns around once, it is also necessary to specify the "sector," as measured with a potentiometer connected to the drive gearbox, to determine the angle absolutely.

The Big Chamber was originally designed for rotation in the horizontal plane. However, the H^- beam at the HiRAB facility may achieve a divergence in the vertical of better than 10^{-5} rad; by turning the chamber on to its side and allowing the plane of intersection of the beams to be vertical also, the low divergence of the particle beam could be used to obtain the optimum resolution. An additional benefit was that the optical alignment was simplified considerably with the chamber on its side.

A pair of polished steel plates with a 1.00-cm separation could be remotely inserted to surround the interaction region. Computer-controlled high-voltage power supplies were used to provide an electrostatic field (up to 100 kV/cm, barycentric frame). One of the plates also had a small fluorescent screen attached to aid in the alignment of the particle beam.

5. Little Chamber

A small scattering chamber was designed and built specifically for a multiphoton detachment experiment.[32] It is described in detail elsewhere.[26]

6. Electron spectrometer

The electron spectrometer uses a magnet to steer electrons out of the ion beam, through a very thin Havar window and into a scintillator. However, sufficiently excited neutral hydrogen atoms are also stripped in the magnetic field (which is perceived as a strong electric field in their rest frame). The electrons produced are then steered into the scintillator. Thus, by changing the field of the spectrometer, we may detect either free—"convoy"—electrons traveling along with the beam, or excited (Rydberg) H^0 atoms. The range of sensitivity of the spectrometer is from $n=10$ upwards. If a slit is used to restrict the entrance aperture of the scintillator, the spectrometer may be tuned to be selectively sensitive to a particular excited state, although there is sufficient overlap of the magnetic substates that the peaks for $n=14$ and above tend to merge. The field in the spectrometer was computer-controlled, and was monitored by a Hall-probe magnetometer.

7. Magnets

There were a number of magnets present in the beamline; each is listed here with a short explanation of its purpose.

(i) HiRAB steering magnets HISM2-X and -Y. These are just upstream of the HiRAB area; they are controlled from the central control room (CCR), in the first instance to steer the beam down our line during the initial tuning, and thereafter under our direction as required to make small corrections to the steering. The long lever arm between these magnets and the interaction region makes them ideal for displacing the beam while minimizing the angular displacement, to which the Doppler-tuning of the lasers is sensitive.

(ii) Vertical steering magnet. Used in conjunction with HISM2Y, this allowed us to make essentially parallel displacements of the H^- beam. It also provided a much more flexible response to changing vertical steering needs, as it was controlled directly from the HiRAB counting house (as were the remaining magnets in our beamline). Another important function served by this and sweep magnet, together with the HISM2 magnets, was to steer the H^- beam clear of the neutral hydrogen

and protons produced upstream by collisions with residual gas.

(iii) Sweep magnet. This magnet provided horizontal steering, and also separated the H^- beam from the residual-gas stripped background beams. Located downstream of the foil boxes, it is also capable of field stripping any high Rydberg atoms produced in the foil; so, if the laser is tuned to excite $H^{0*}(n=4)$ to $H^{0*}(n=16)$, say, we can be sure that the $H^{0*}(n=16)$ states we detect in the electron spectrometer are not foil produced.

(iv) Ionization magnet. Designed to produce a strong horizontal magnetic field over a short region of space, i.e., a large **B** with a small $\int \mathbf{B}\cdot d\mathbf{l}$, this magnet could strip the electrons from laser-excited neutral hydrogen atoms of $n=6$ and above, while minimizing the steering of the beam. It had a compensating pole piece to offset any steering that did take place; furthermore, because the field was horizontal, it steered only in the vertical plane, to which our detectors were not especially sensitive.

(v) Bending magnets. These magnets performed the same function as the ionization magnet, but their higher fields (approximately 4 kG) allowed stripping of $H^0(n=4)$. Their residual fields were too large for the higher Rydberg states, and so they were removed from the beamline when necessary and the ionization magnet was used instead.

(vi) Long Skinny magnet. In order to study the double-detachment threshold, a means of separating the signal protons from neutral hydrogen atoms without field ionizing the highly excited neutrals was required. A long magnet was therefore employed, the weak field of which could gently separate the three charge species. This magnet consisted of four copper rods running parallel to the beamline, each on the corner of a square concentric with the beam line as viewed in cross section; each rod, 21 ft long, carried a current so as to produce a vertical (upward) magnetic field. The arrangement resembles an extremely stretched pair of Helmholtz coils, as illustrated in Fig. 5. In reality, background problems limited the threshold study, so this magnet was usually run at a fairly high current in order to maximize the separation of the three beams.

As mentioned above, with the exception of the HISM steering magnets, all of these magnets, in addition to the electron spectrometer, were controlled from the HiRAB counting house. The latter two magnets—the Long Skinny magnet and the bending magnets—were powered by a Dual Transrex high current supply (up to 750 and 500 amps, respectively).

8. Detectors

Photomultiplier tubes in combination with fast organic scintillators were used for detection of electrons, protons, and neutral hydrogen atoms. Both the H^+ and H^0 detectors were on actuators that allowed remote positioning in the transverse horizontal direction; in the case of the H^+ detector, the scintillator itself was in the vacuum, and a light guide passed through the vacuum seal to the photomultiplier.

In anticipation of the need for a wide dynamic range—a single pulse might contain one signal particle, or it might contain a hundred or more—highly linear phototubes (Amperex XP2203B) were obtained. Details of the tube and of the base circuit are published elsewhere.[26]

The H^0 detector, which was outside the vacuum (the H^0 beam had to pass through a Havar window before reaching the scintillator), had a phototube at either end of the scintillator, one being kept at a higher voltage than the other to give a still wider dynamic range.

9. Beam-current monitors

The photodetachment yield is obviously directly proportional to the current of the H^- beam; it is therefore important to monitor both short- and long-term fluctuations in the beam current. The primary normalization to beam current is done with a Faraday cup.[33] The absolute charge-collection efficiency of this device is better than 1%. A current digitizer (Ortec model CD 1010) emits a pulse whenever the cup collects 100 pC. During the experiment, the angle of intersection of laser and particle beam was changed whenever the number of such pulses reached a preset figure.

The Faraday cup measures integrated current, for online normalization; however, it is also important to account for pulse-to-pulse variations in intensity. For this purpose, we employ a fast ion chamber (FIC), which contains three wire grids at high voltage in a hydrogen-filled container;[34] as the beam travels through, the ions produced create a shower, generating a current which passes through a resistive load. A voltage-to-frequency converter then puts out a series of pulses that are counted by a scalar in a CAMAC crate to provide a measure of beam current on the time scale of a macropulse.

In addition, a scintillator-phototube combination (the "paddle") allowed observation of individual micropulses. In the end, this latter method proved somewhat unreliable; we believe that the scintillator was unable to respond properly to, and may in fact have been damaged by, the full current of the H^- beam, which was focused to a spot only 2–3 mm in diameter. However, it was still useful for providing timing information, and to confirm the presence of the micropulses.

10. Vacuum Pumps and Gauges

In order to minimize backgrounds from collisional stripping of H^- by residual gas, it was necessary to keep the pressure down to the 10^{-7}–10^{-8}-Torr range. Although the only vacuum gauges available to us were cold cathode gauges, which were not capable of measuring below 10^{-7} Torr, fairly low currents in the three ion pumps in the line—one by the foil boxes, one on the Little Chamber, and one downstream of the skinny magnet—assured us that the vacuum was in fact in the desired range. In addition, two cryogenic pumps were employed, also attached to the Little Chamber and to the beam pipe downstream of the skinny magnet.

APPENDIX B: DATA REDUCTION

1. Normalization of signals

As discussed elsewhere,[26] in order to obtain the relative cross section from the count rate, the signal must be multiplied by a factor of $\sin\alpha/(1+\beta\cos\alpha)$. However, in the case of the resonances, an alternative form of normalization was available; the cross section for the production of the H^0 atoms stays relatively constant over the photon-energy range under consideration, and so the H^0 signal automatically includes the normalizing factor, in addition to any fluctuations that may be related to changes in the laser or in the particle beam.

Before normalization to the H^0 signal could take place, it was necessary to subtract any backgrounds present in both the H^+ and H^0 channels. This was sometimes difficult because, although several runs included signals taken at a few angles with the laser blocked, not all did; it was not obvious at the time that the background levels were changing, sometimes slowly drifting up or down and sometimes jumping.

Each of the two signal channels (H^+ and H^0) had a background channel associated with it. By looking at the H^0 signal for the periods where the laser was blocked, and comparing it with the average value for the H^0 background (i.e., data taken during the background gate), it was determined that the background count rate needed to be multiplied by 2.4 ± 0.1 in order to make it compatible with the true background levels in the H^0 signal channel. The uncertainty in this ratio is a systematic error, and so is not included in the error bars, which are purely statistical, as discussed later.

A similar subtraction of backgrounds was required from the H^+ signal channel. The cross section, of course, dropped to zero below threshold, in which case the background level could be determined even when the laser was not blocked. The relevant ratio between background levels in the signal and background channels again fluctuated significantly, but the signal-to-background ratio was much smaller (often less than 1), making these fluctuations more important. A different approach was therefore adopted here. First, a particularly "clean" run, where all conditions were stable throughout the run, was chosen for each of the hydrogenic excited-state channels studied—$n=4$, 5, 6, 7, and 8. These runs also had to cover the entire energy range for the relevant channel, including some data points below the threshold, for which the true signals would be zero. (Many runs did not include such regions, and so did not have clearly defined background levels.) The background subtraction was done for each of these sets of data as for the H^0 signals, and the H^+ signals were then normalized to the H^0 channel for these runs.

The "master" data files produced in this manner were used for scaling all of the other (zero field) runs, so that comparisons could fairly be made between runs taken at different beam currents, with different backgrounds and so on. Fitting of the the scale factors between the data sets allowed the background levels to be determined for those runs for which they would otherwise have been unobtainable. With the backgrounds subtracted, each run could then be normalized to its H^0 signal and scaled appropriately to produce the relative cross section.

$1/n^3$ scaling

The actual distribution of excited neutral hydrogen states is expected to obey a $1/n^3$ power law, where n is the principal quantum number. In other words, for every $H^0(n=2)$ atom, eight $H^0(n=1)$ atoms would be produced; for every $H^0(n=3)$, 27 $H^0(n=1)$ atoms and so on. (As the double-detachment threshold is approached, however, a Wannier-type power law, $\sigma\propto(E_t-E)^{1.127\cdots}$, where E_t is the double-detachment threshold energy, is believed to become dominant). Although no attempt was made at the time to determine the actual ratios of production of the successive n channels, later analysis shows production of $n=4$ to $n=5$ in the ratio of approximately 1.35, and $n=5$ to $n=6$ in the ratio of 1.75; these are to be compared with the expected ratios from the $1/n^3$ law of 1.95 and 1.72, respectively. This would seem to indicate that the $1/n^3$ law applies, but that the magnets were not perfectly efficient in stripping $n=4$; this is to be expected with a 4-kG field.

The cross section for production of $H^0(n=1)$ in this energy range is approximately $0.13a_0^2$. On the basis of this, and the $1/n^3$ law, a multiplicative factor was applied throughout each data file, so that the units labeled "arbitrary" in the figures showing relative cross sections versus energy should in fact be units of approximately $10^{-6}a_0^2$.

2. Calculation and propagation of uncertainties

Propagation of error bars was the cause of some concern. Initially, when the backgrounds were subtracted, the uncertainties were added in quadrature; and when the normalization to the H^0 channel was done, the relative uncertainties were added, again in quadrature. Such is the normal procedure—for data that are independent. However, there are of course strong correlations between the fluctuations in the H^+ and H^0 signals—it is for this reason that we normalize to the H^0 channel in the first place. The error bars were therefore too large and needed to be recalculated.

The mean signal $\bar{x}$ per laser shot is simply given by

$$\bar{x}=\frac{\sum x}{N}\ , \tag{B1}$$

where N is the number of laser shots (usually 100–200 for the Nd:YAG laser) per angle. The standard deviation of this mean is σ, where

$$\sigma_x^2=\left[\frac{\sum(x-\bar{x})^2}{N(N-1)}\right]^{1/2} \approx\left[\frac{(\bar{x}^2-\bar{x}^2)}{N}\right]^{1/2}. \tag{B2}$$

Although of course the mean signal per laser shot is proportional to the beam current (since the higher the

current, the more photodetachments occur in each pulse), normalizing to the H^0 signal removes this dependence.

Given some function $S=S(x,y)$ the uncertainty in S is obtained from the uncertainties $\delta x=\sigma_x$, $\delta y=\sigma_y$ by a Taylor expansion of S evaluated at $\bar{x},\bar{y}$:

$$\sigma_S^2=\left[\frac{\partial S}{\partial x}\right]^2\sigma_x^2+\left[\frac{\partial S}{\partial y}\right]^2\sigma_y^2+2\left[\frac{\partial S}{\partial x}\right]\left[\frac{\partial S}{\partial y}\right]\sigma_{xy}^2 . \quad \text{(B3)}$$

The third term accounts for correlations between the quantities x and y; it is generally close enough to zero to be ignored when x and y are totally independent, but in our case the signal and background channels will have correlated fluctuations if there are fluctuations in the beam current, and the H^+ and H^0 signals will also have significant correlations if there are fluctuations in the laser power. The factor σ_{xy} is calculated, in a manner analogous to σ_x and σ_y, by the formula

$$\sigma_{xy}^2=\frac{\sum(x-\bar{x})(y-\bar{y})}{N(N-1)} . \quad \text{(B4)}$$

In our case, $S=x-y$, and the uncertainty in the net signal after background subtraction (in both the H^+ and H^0 channels) is

$$\sigma_S=(\sigma_x^2+\sigma_y^2-2\sigma_{xy}^2)^{1/2} , \quad \text{(B5)}$$

where x and y are the values from the signal and background channels, respectively. The normalization of the H^+ signal S_+ to the H^0 signal S_0, giving a total signal $S_{+/0}=S_+/S_0$, then requires further propagation of these uncertainties, thus [from Eq. (B3)]

$$\left[\frac{\sigma_{+/0}}{S_{+/0}}\right]^2=\frac{\sigma_+^2}{S_+^2}+\frac{\sigma_0^2}{S_0^2}-2\frac{\sigma_{+0}^2}{S_+S_0} . \quad \text{(B6)}$$

The resulting error bars represent the true statistical fluctuations in the signals. This method is in contrast to our usual procedure of estimating the number of particles in each pulse from a pulse-height analysis, and assuming Poisson statistics, where the mean fluctuation in the number of particles is simply equal to the square root of that number. Since the H^+ detector did not give clearly resolved peaks for single, double, triple, and other multiple counts (the individual particle signals were too small), it was impossible to calculate the multiplicity of hits.

The error bars do not give any indication of systematic uncertainties. These would tend to smear out all of the error bars by the same amount. Since fitting routines assume that the error bars represent only statistical fluctuations, possible systematic errors—for example, uncertainty in the overall background levels—have not been included.

Once the data files from the individual runs had been prepared, they were binned together to produce the data sets seen in Figs. 8(a)–8(d). Within each bin, a weighted average was taken in the normal way, producing a net signal

$$y=\frac{\sum_i y_i/\sigma_i^2}{\sum_i 1/\sigma_i^2} \quad \text{(B7)}$$

with its standard deviation

$$\sigma=\left[\sum_i \frac{1}{\sigma_i^2}\right]^{1/2} . \quad \text{(B8)}$$

The bin sizes were adjusted so that in each case the energy range covered included about 80–100 data points (just as the angular step size was adjusted during the actual runs for the same reason).

3. Fitting

The fitting routine used here was MINUIT,[35] a powerful package developed at CERN, that uses several different methods to minimize a specified quantity; for this analysis, the quantity used was χ^2, defined as

$$\chi^2=\sum_i\left[\frac{f(x)-d_i(x)}{\sigma_i}\right]^2 , \quad \text{(B9)}$$

where $d_i(x)$ are the data points with uncertainties σ_i and $f(x)$ is the function (with up to 30 parameters, up to 15 of which may be varied at once) to which the data are being fit.

In the case of the resonances on the continuum background, each resonance has an amplitude (see Sec. I F).

$$\psi_R(E)=\frac{ia\Gamma/2}{E-E_0+i\Gamma/2} , \quad \text{(B10)}$$

and a phase difference ϕ with the continuum on which it lies. The amplitude of the continuum was modeled as linearly increasing with photon energy. Thus, the total amplitude for a series of n resonances is

$$\psi_t(E)=b+cE+\sum_{k=1}^{n}\frac{ia_k e^{i\phi_k}}{i+2(E-E_{0_k})/\Gamma_k} , \quad \text{(B11)}$$

where the factor of $\Gamma/2$ in the numerator of Eq. (B10) has been included in the constant a_k. The function $f(x)$ is then given by the cross section (or intensity),

$$f(x)=\sigma(x)=\psi^*\psi . \quad \text{(B12)}$$

Usually, three resonances were used to model the data; because each has an amplitude, a phase, a width and a centroid, there would be 12 free parameters together with another two for the continuum background and slope. When MINUIT had made reasonable estimates of the parameters of the continuum and of the largest of the resonances, these could be "fixed" and a fourth resonance added in for "fine tuning." In no case were more than four dips visible in one channel.

It emerged that the resonances were narrow enough (in comparison with their spacing) that there was little danger of their overlapping; in this case, the intensities could be added directly (rather than adding the amplitudes), and so they were also fit to sets of the more standard Fano profile,

$$\sigma=\sigma_b+\sum\sigma_a\left[\frac{(q+\varepsilon)^2}{1+\varepsilon^2}-1\right] . \quad \text{(B13)}$$

The σ_b here is a little different from that of the usu

Fano profile, since an extra σ_a has been subtracted from it [see Eq. (34)], and it is also assumed to have a linear energy dependence. Note that there is a slight difference here from the "coherent amplitude" model, in which the *amplitude* of the background continuum was assumed to be a linear function of the photon energy [$b+cE$ in Eq. (B11)].

In addition, the widths and energies of each series of resonances (in each hydrogenic n continuum channel) were fit to the recursion formula (see Sec. I D)

$$\frac{E_n-E_k}{E_n-E_{k+1}}=e^{-2\pi/\alpha}=\frac{\Gamma_k}{\Gamma_{k+1}} . \tag{B14}$$

Section III contains additional discussion of the fits carried out, together with their results.

---

*Present address: University of Illinois at Urbana-Champaign, Nuclear Physics Laboratory, 23 Stadium Drive, Champaign, IL 61820.

[1]P. G. Harris, H. C. Bryant, A. H. Mohagheghi, R. A. Reeder, H. Sharifian, H. Tootoonchi, C. Y. Tang, J. B. Donahue,* C. R. Quick, D. C. Rislove, W. W. Smith, Phys. Rev. Lett. **65**, 309 (1990).
[2]J. Macek, J. Phys. B **1**, 831 (1968).
[3]C. D. Lin, Adv. At. Mol. Phys. **22**, 77 (1986).
[4]C. D. Lin, Phys. Rev. A **10**, 1986 (1974).
[5]A. R. P. Rau, in *Atoms In Unusual Situations*, edited by J. P. Brown (Plenum, New York, 1987).
[6]R. P. Madden and K. Codling, Phys. Rev. Lett. **10**, 516 (1963).
[7]J. W. Cooper, U. Fano, and F. Prats, Phys. Rev. Lett. **10**, 518 (1963).
[8]H. C. Bryant, B. D. Dieterle, J. Donahue, H. Sharifian, H. Tootoonchi, D. M. Wolfe, P. A. M. Gram, and M. A. Yates-Williams, Phys. Rev. Lett. **38**, 228 (1977).
[9]H. R. Sadeghpour and C. H. Greene, Phys. Rev. Lett. **65**, 313 (1990).
[10]H. R. Sadeghpour (private communication).
[11]C. H. Greene, J. Phys. B **13**, L39 (1980).
[12]C. D. Lin, Phys. Rev. Lett. **51**, 1348 (1983).
[13]C. D. Lin, Phys. Rev. Lett. **35**, 1150 (1975).
[14]H. C. Bryant, David A. Clark, Kenneth B. Butterfield, C. A. Frost, H. Sharifian, H. Tootoonchi, J. B. Donahue, P. A. M. Gram, M. E. Hamm, R. W. Hamm, J. C. Pratt, M. A. Yates, and W. W. Smith, Phys. Rev. A **27**, 2889 (1983).
[15]D. R. Herrick and Sinanoglu, Phys. Rev. A **11**, 97 (1975).
[16]Y. K. Ho and J. Callaway, Phys. Rev. A **34**, 130 (1986).
[17]M. Gailitis and R. Damburg, Zh. Eksp. Teor. Fiz. **44**, 1644 (1963) [Sov. Phys.—JETP **17**, 1107 (1963)].
[18]F. H. Read, Aust. J. Phys. **35**, 475 (1982).
[19]A. R. P. Rau, J. Phys. B **16**, L699 (1983).
[20]Q. Molina, Phys. Rev. A **39**, 3298 (1989).
[21]A. R. P. Rau, Phys. Rev. A **4**, 207 (1971).
[22]M. E. Hamm, R. W. Hamm, J. Donahue, P. A. M. Gram, J. C. Pratt, M. A. Yates, R. D. Bolton, D. A. Clark, H. C. Bryant, C. A. Frost, and W. W. Smith, Phys. Rev. Lett. **43**, 1715 (1979).
[23]U. Fano, Phys. Rev. **124**, 1866 (1961).
[24]C. A. Frost, Ph.D. dissertation, University of New Mexico, 1981 (Los Alamos Report No. LA-8976-T).
[25]D. A. Clark, H. C. Bryant, K. B. Butterfield, C. A. Frost, J. B. Donahue, P. A. M. Gram, M. E. Hamm, R. W. Hamm, and W. W. Smith, Bull. Am. Phys. Soc. **9**, 1137 (1980).
[26]P. G. Harris, Ph.D. dissertation, University of New Mexico (Los Alamos Report No. LA-11843-T).
[27]P. G. Harris, H. C. Bryant, A. H. Mohagheghi, C. Y. Tang, J. B. Donahue, C. R. Quick, R. A. Reeder, J. E. Stewart, T. Altman, and D. Rislove, Nucl. Instrum. Methods A **292**, 254 (1990).
[28]C. H. Green (private communication).
[29]Y. K. Ho, Phys. Rev. A **41**, 1492 (1990).
[30]Naoto Koyama, Atusko Takafuji, and Michio Matsuzawa, J. Phys. B **22**, 553 (1989).
[31]John McGill (private communication).
[32]C. Y. Tang, P. G. Harris, A. H. Mohagheghi, H. C. Bryant, C. R. Quick, J. B. Donahue, R. A. Reeder, Stanley Cohen, W. W. Smith, J. E. Stewart, Phys. Rev. A **39**, 6068 (1989).
[33]R. J. Barrett, B. D. Anderson, H. B. Willard, A. N. Anderson, and N. Jarmie, Nucl. Instrum. Methods **129**, 441 (1975).
[34]V. Yuan (private communication).
[35]F. James and M. Roos, Comput. Phys. Commun. **10**, 343 (1975).